






Observing Planet-driven Dust Spirals with ALMA

Jessica Speedie¹ , Richard A. Booth² , and Ruobing Dong (董若冰)¹ ¹Department of Physics & Astronomy, University of Victoria, Victoria, BC, V8P 1A1, Canada; jspeedie@uvic.ca, rbdong@uvic.ca²Astrophysics Group, Imperial College London, Prince Consort Road, London, SW7 2AZ, UK

Received 2021 October 29; revised 2022 February 12; accepted 2022 February 28; published 2022 May 3

Abstract

Atacama Large Millimeter/submillimeter Array (ALMA) continuum observations of thermal emission from the dust component of protoplanetary disks have revealed an abundance of substructures that may be interpreted as evidence for embedded planets, but planet-driven spiral arms—perhaps one of the most compelling lines of evidence—have proven comparatively elusive. In this work, we test the capabilities of ALMA to detect the planet-driven spiral signal in continuum emission. Carrying out hydrodynamic simulations and radiative transfer calculations, we present synthetic Band 7 continuum images for a wide range of disk and observing conditions. We show that thermal mass planets at tens of astronomical units typically drive spirals detectable within a few hours of integration time, and the detectable planet mass may be as low as \sim Neptune mass ($0.3 M_{\text{th}}$). The grains probed by ALMA form spirals morphologically identical to the underlying gas spiral. The temperature of the dust spiral is crucial in determining its contrast, and spirals are easier to detect in disks with an adiabatic equation of state and longer cooling times. Resolving the spiral is not necessary for its detection; with the help of residual maps, the optimal beam size is a few times the spiral width at a constant noise level. Finally, we show how the presence of gaps and rings can impair our ability to recognize colocated spirals. Our work demonstrates the planet-finding potential of the current design specification of ALMA, and suggests that observing capability is not the bottleneck in searching for spirals induced by thermal mass planets.

Unified Astronomy Thesaurus concepts: [Planet formation \(1241\)](#); [Protoplanetary disks \(1300\)](#); [Planetary-disk interactions \(2204\)](#)

1. Introduction

Like the wake created by a boat as it moves through water, a planet drives a wake as it orbits in a disk (Ogilvie & Lubow 2002). The wake then gets wound into a spiral by the disk’s own Keplerian differential rotation (Arzamasskiy & Rafikov 2018). Planet-driven spiral arms are a well-understood natural consequence of the gravitational interaction between the planet and the disk; the analytical theory was established in the 1970s (Goldreich & Tremaine 1978, 1979, 1980) and has been repeatedly confirmed by hydrodynamical simulations (Dong et al. 2011a, 2011b; Zhu et al. 2015; Bae & Zhu 2018a, 2018b; Miranda & Rafikov 2019a). We therefore expect that within every planet-hosting protoplanetary disk, spiral wakes should also exist.

This theoretical expectation has not translated into an abundance of clear observational detections of planet-driven spirals, however. That statement particularly applies to continuum observations of (sub-)millimeter dust. High angular resolution Atacama Large Millimeter/submillimeter Array (ALMA) continuum observations have shown that gaps and rings are common (e.g., Huang et al. 2018a), implying an abundance of planets forming in disks (Zhang et al. 2018), but to date we have only a handful of detections of continuum spirals. Elias 27, IM Lup, and WaOph 6 (Huang et al. 2018b) exhibit large-scale $m = 2$ continuum spirals, but they are not colocated with a gap/cavity, and have not been decisively attributed to an embedded companion (Mawet et al. 2012; Meru et al. 2017; Paneque-Carreño et al. 2021; Brown-Sevilla et al. 2021). A smaller scale, single continuum spiral has been observed in

MWC 758 (Dong et al. 2018c); the motion of that disk’s related $m = 2$ scattered light spirals have been reported as inconsistent with gravitational instability (Ren et al. 2020) but no associated point source has yet been detected (Boccaletti et al. 2021). Tentative crescents or filaments in association with gaps/rings have been observed in continuum images of V1247 Ori (Kraus et al. 2017) and HD 135344B (Casassus et al. 2021) but have not been confidently classified as spirals. Continuum spirals in disk systems with multiple stars, HD100453 (Rosotti et al. 2020), AS 205 N, and HT Lup A (Kurtovic et al. 2018) have been identified as induced by gravitational interaction with companions, but the companions are not of planetary mass.

Searches for planet-driven dust spirals in continuum observations, and recognizing the signatures that a spiral is planet driven if it is found, would benefit from a clearer understanding of the following complexities:

1. It is well understood how planets drive spirals in the gas, but it is not necessarily obvious how spirals manifest in the dust. The morphology (i.e., the amplitude, width, and azimuthal location) of dust spirals is determined by how quickly each particle responds to the drag forces exerted by the passing spiral wake (Sturm et al. 2020). The response time of the dust depends on how well it is coupled to the gas, which in turn depends on the grain properties and local gas density (the latter making it a function of radial location and height above the midplane, e.g., Equation (1) of Veronesi et al. 2019). For each observing wavelength and instrument, we need to understand what architecture of dust spiral we are looking for.
2. Compounding this is the fact that planet-driven spirals are not dust traps. Since the gas spiral wake comoves with the planet as it orbits the star, the dust experiences the spiral



Original content from this work may be used under the terms of the [Creative Commons Attribution 4.0 licence](#). Any further distribution of this work must maintain attribution to the author(s) and the title of the work, journal citation and DOI.

perturbation as a transient phenomenon. As a result, a dust spiral’s density amplitude cannot exceed that of the gas. This is different to the case of dust rings, where dust can accumulate in a stationary (or at least, long-lived) pressure maximum over time (Whipple 1972). In this way, a lower mass planet can still produce readily detectable dust gaps/rings (e.g., Rosotti et al. 2016; Bae et al. 2017; Dong et al. 2017, 2018a), but a lower mass planet drives proportionally lower amplitude spiral arms (Dong et al. 2011b; Bae & Zhu 2018a; Miranda & Rafikov 2019a). We need to understand what level of contrast a planet-driven spiral can achieve in the dust density for planets in the *still-forming* mass range.

3. How we can actually observe the dust density distribution is, in the case of continuum observations, through its thermal emission—which then introduces the question of dust temperature and the rate at which the disk cools. The importance of using a realistic treatment of disk thermodynamics in simulations whose purpose is to interpret or predict planet-induced disk substructure is gaining recognition (Miranda & Rafikov 2019b). One’s choice of the equation of state has been shown to have significant consequences on the density wave dynamics (Miranda & Rafikov 2020a). The rate of cooling, specifically, affects the angular momentum flux across the disk, which modifies the gas spiral density amplitude (Miranda & Rafikov 2020b; Zhang & Zhu 2020). The hydrodynamic PdV work done on the gas as the spiral pressure wave passes generates a rise in the temperature distribution, forming temperature spirals whose amplitudes can be observationally significant (Muley et al. 2021). For a given disk’s thermodynamic properties (and optical depth), we need to understand how the density and temperature spirals combine into the observed quantity of intensity—for the dust.
4. Finally, there is the practical consideration of the angular resolution and sensitivity at which we observe. Once we understand the dust spiral morphology and possible intensity contrast, we can establish which observing specifications, and which disks, give us the best chance of detecting planet-driven dust spirals.

In this work, we carry out this experiment for the case of submillimeter dust continuum observations with Band 7 of ALMA. Our purpose is to aid searches for planet-driven dust spirals in existing ALMA observations and to inform future observing proposals.

Section 2 describes our methodology. In Section 3, we present our results on the important physics: dust-gas coupling (Complexities 1 and 2) and thermodynamics (Complexity 3). In Section 4 (Complexity 4), we present synthetic ALMA continuum observations of planet-driven dust spirals for a variety of disk and observing conditions. We discuss our results in Section 5 and summarize our findings in Section 6.

2. Methods

We run 2D gas + dust hydrodynamic simulations of disks with different cooling rates, optical depths, and embedded planet masses to obtain the dust density and temperature distributions at the disk midplane (Section 2.1). The dust grain size is fixed to $a_{\text{grain}} = 0.14$ mm to correspond to Band 7 and the gas surface density is varied to achieve different dust optical depths assuming a fixed dust-to-gas mass ratio of 0.01.

Next, we create synthetic continuum emission images of the resulting dust spirals via radiative transfer calculations (Section 2.2). With those we generate synthetic ALMA observations for a range of integration times and antenna configurations (Section 2.3). Figure 1 provides examples of the outputs after each step of our procedure.

2.1. Hydrodynamic Simulations

We perform 2D multi-fluid hydrodynamic simulations with a custom version of the FARGO3D code (Benítez-Llambay & Masset 2016), modified to compute dust dynamics with the Eulerian implementation described in Rosotti et al. (2016), which uses the semi-implicit integrator introduced by Booth et al. (2015).

We run the simulations in a 2D cylindrical geometry (r, ϕ) . The units are dimensionless, such that the orbital radius of the planet (r_p) is unity, the unit of time is the Keplerian angular velocity Ω_{Kep} at $r = r_p$, and the unit of mass is that of the central star. The domain extends from 0.1–3.0 r_p in radius and from $-\pi$ to π in azimuth. The grid has a resolution of $N_r \times N_\phi = 1100 \times 2048$ cells, spaced logarithmically and linearly in the radial and azimuthal directions, respectively, for approximately square cells. With this resolution, one scale height at r_p is resolved with 23 cells in both directions, and we resolve the spiral shock fronts.

The code solves the mass, momentum, and energy equations of hydrodynamics:

$$\frac{\partial \Sigma_{\text{gas}}}{\partial t} + \nabla \cdot (\Sigma_{\text{gas}} \mathbf{v}_{\text{gas}}) = 0, \quad (1)$$

$$\frac{\partial \mathbf{v}_{\text{gas}}}{\partial t} + \mathbf{v}_{\text{gas}} \cdot \nabla \mathbf{v}_{\text{gas}} + \frac{\nabla P}{\Sigma_{\text{gas}}} = \mathbf{g}, \quad (2)$$

$$\frac{\partial E}{\partial t} + \mathbf{v}_{\text{gas}} \cdot \nabla E + \frac{P}{\Sigma_{\text{gas}}} \nabla \cdot \mathbf{v}_{\text{gas}} = 0, \quad (3)$$

where Σ_{gas} , \mathbf{v}_{gas} , P , and E are the gas surface density, velocity, pressure, and internal energy per unit area, and \mathbf{g} is the gravity term.

We solve the energy equation for the gas and simultaneously evolve the dust.³ The dust is treated as a pressureless fluid and evolves according to linear drag forces from the gas, in addition to gravity and diffusion. The dust velocity is given by

$$\frac{d\mathbf{v}_{\text{dust}}}{dt} + \mathbf{v}_{\text{dust}} \cdot \nabla \mathbf{v}_{\text{dust}} = -\frac{1}{t_{\text{stop}}}(\mathbf{v}_{\text{dust}} - \mathbf{v}_{\text{gas}}(t)) + \mathbf{a}_{\text{dust}}, \quad (4)$$

where t_{stop} is the stopping time of the dust and \mathbf{a}_{dust} is the non-drag acceleration. We focus on dust with dimensionless stopping time $t_{\text{stop}} \Omega_{\text{Kep}} \leq 1$, for which the fluid approximation is reasonable (Garaud et al. 2004). Throughout our simulations the dust-to-gas ratio never approaches unity, thus the back-reaction from the dust onto the gas is unimportant and ignored. We include dust diffusion, and the Schmidt number (the ratio of the α -viscosity ν to the dust diffusion coefficient D) is set to $\text{Sc} = \nu/D = 1$.

In order to explore the observability of planet-driven dust spirals in a diversity of disk conditions, we vary the gas equation of state to be locally isothermal or adiabatic. The relationship between the gas pressure, density, and temperature

³ To our knowledge, ours is the first work using this custom version of FARGO3D to do so.

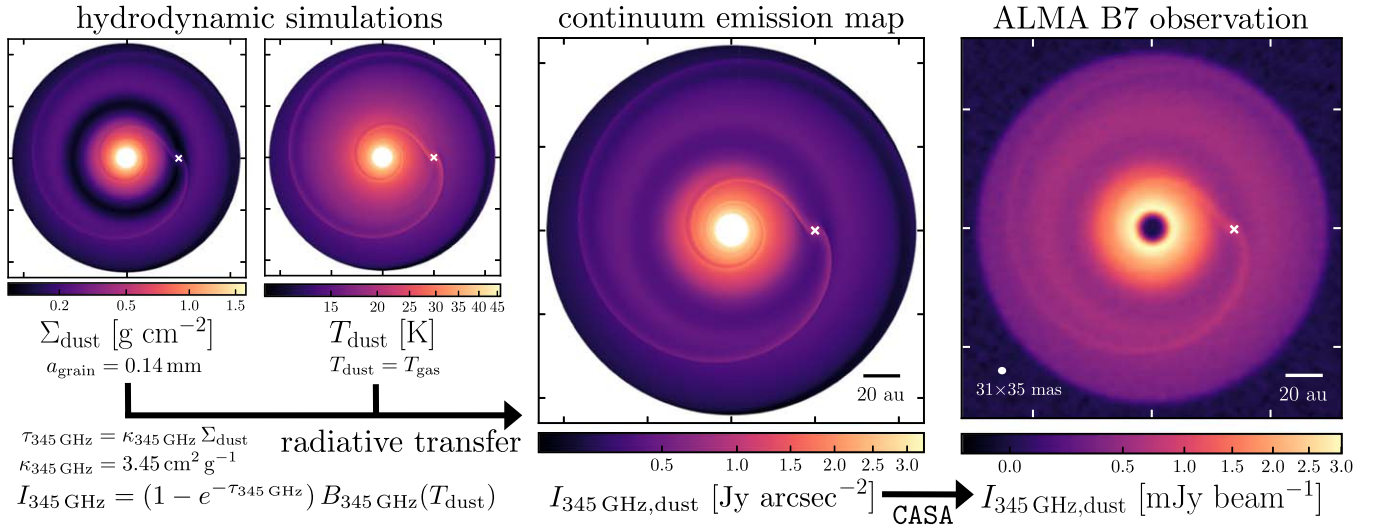


Figure 1. The procedure by which we generate synthetic ALMA continuum observations of planet-driven spiral arms. Dust surface density and temperature maps from our hydrodynamic simulations are combined via radiative transfer calculations to create model images of dust thermal emission (emergent intensity), with which we generate continuum observations using *CASA*. Shown here is the case of a $1 M_{\text{th}}$ planet embedded in an adiabatic ($\beta = 10$), marginally optically thick disk ($\tau_0 = 1.0$), observed with the C43-5 + C43-8 configuration pair and a combined 8.0 hr of on-source time (measured rms noise $9.17 \mu\text{Jy beam}^{-1}$).

naturally affects the gas spiral, which in turn we expect to affect the resultant dust spiral via dust-gas coupling.

The adiabatic equation of state is $P = (\gamma - 1)E$, and the gas temperature is

$$T_{\text{gas,adi}} = \frac{\mu m_p (\gamma - 1) E}{k_B \Sigma_{\text{gas}}}. \quad (5)$$

Here, $\mu = 2.3$ is the mean molecular weight of a fully molecular gas of cosmic composition (mix of H and He), m_p is the mass of a proton, k_B is the Boltzmann constant, and γ is the adiabatic index. In this work, we assume $\gamma = 5/3$, appropriate for a composition of H_2 at a low temperature (tens of Kelvin). We perform the adiabatic simulations with a simple cooling prescription, such that the gas temperature is relaxed toward its initial state on a timescale controlled by the parameter β :

$$\frac{dE(t)}{dt} = -\frac{\Omega}{\beta} (E(t) - E_0), \quad (6)$$

where Ω is the local angular velocity. Previous work has shown that simulations with an adiabatic equation of state and short cooling times ($\beta \lesssim 10^{-1}$) yield small planet-induced temperature perturbations and are very similar to simulations with an isothermal equation of state (Miranda & Rafikov 2020b, 2020a; Zhang & Zhu 2020; Muley et al. 2021). Analytic expressions derived assuming conventional dust properties indicate that the cooling timescale can vary dramatically within a single disk at different radii, and typical values are $t_{\text{cool}} = \beta \Omega^{-1}(r) \sim 20$ at $r = 10 \text{ au}$ and $t_{\text{cool}} \sim 0.02$ at $r = 100 \text{ au}$ (Equation (39) of Zhang & Zhu 2020). Thus, in our experiments we explore β values of 0 (isothermal) and 10. We note that while the code does not add the energy dissipated via physical viscosity (e.g., α viscosity) to the internal energy of the gas, the heating due to the artificial viscosity (for handling shocks) has been included.⁴

⁴ Viscous heating is also missing in the public version of *FARGO3D* (Benítez-Llambay & Masset 2016).

Viscous heating is likely unimportant for our purposes as we are modeling Class II disks with planets at tens of astronomical units.

We initialize the aspect ratio in the disk as

$$h(r) = H/r = h_p r^f, \quad (7)$$

where we choose a flaring index of $f = 1/4$ and value of h at the location of the planet $h_p = 0.07$ (see Section 2.2 for physical motivation). We use the α viscosity prescription of Shakura & Sunyaev (1973) and assume the conventional $\alpha = 10^{-3}$. Varying the viscosity does not impact the spiral arms (Dong & Fung 2017), while it makes an impact on the gap depth (Fung et al. 2014).

We tailor the setup of the dust component of our hydrodynamic simulations toward the end goal of ALMA Band 7 continuum observations by fixing the dust grain size. For the observing wavelength $\lambda_{\text{obs}} = 0.87 \text{ mm}$ (observing frequency $\nu_{\text{obs}} = 345 \text{ GHz}$), we assume we probe thermal emission from dust particles of size (Kataoka et al. 2015; Pavlyuchenkov et al. 2019)

$$a_{\text{grain}} \approx \frac{\lambda_{\text{obs}}}{2\pi}, \quad (8)$$

giving a dust grain size of $a_{\text{grain}} = 0.14 \text{ mm}$. This means that the dust Stokes number,

$$\text{St} = t_{\text{stop}} \Omega_{\text{Kep}} = \frac{\pi a_{\text{grain}} \rho_{\text{dust}}}{2 \Sigma_{\text{gas}}}, \quad (9)$$

varies in space and time inversely to the gas surface density. We assume $\rho_{\text{dust}} = 1.2 \text{ g cm}^{-3}$ for the bulk grain density (in broad agreement with Birnstiel et al. 2018). The initial gas surface density distribution is assumed to follow a power law

$$\Sigma_{\text{gas}}(r) = \Sigma_0 \left(\frac{r}{r_p} \right)^{-1}, \quad (10)$$

where Σ_0 is the initial gas surface density at $r = r_p$. Since the simulations are scale-free and we ignore dust feedback, the

normalization factor Σ_0 is arbitrary and we can use Σ_0 to scale our simulation results during post-processing to the physical Σ_{gas} and St that matches the a_{grain} we desire. More on this in Section 2.2.

We run our simulations with three different planet masses: $M_p = 0.3, 1.0,$ and $3.0 M_{\text{th}}$ (where the thermal mass is $M_{\text{th}} = h^3 M_*$), corresponding to planet-star mass ratios of $q = 1.03 \times 10^{-4}, 3.43 \times 10^{-4},$ and 1.03×10^{-3} . With an aspect ratio of $h_p = 0.07$ and a stellar mass of $M_* = 0.8 M_\odot$, those masses equate to $1.6 M_{\text{Nep}}, 0.96 M_{\text{Sat}},$ and $0.86 M_{\text{Jup}}$ respectively. We keep the planet on a fixed circular orbit and include the indirect term that compensates for the displacement between the simulation grid origin and the star–planet center of mass. We simulate to 1500 orbits so that gaps and rings, a commonly observed category of disk substructure, have fully formed (e.g., Figure 1, Fung & Chiang 2016).

In addition to the simulations that we use to generate ALMA observations (presented in Section 4), we run a separate shorter set (15 orbits) for the purposes of deepening our understanding the effect of the cooling time and dust-gas coupling on the spiral’s intrinsic properties (presented only in Sections 3.1 and 3.2). In this set, we vary the cooling time from $\beta = 10^{-3}$ – 10^2 in factors of 10. Following Sturm et al. (2020), we evolve 40 species of dust with a spatially and temporally constant Stokes number logarithmically spaced between $\text{St} = 10^{-4}$ and 1.0. Otherwise, the simulation setup is the same.

2.1.1. Boundary Conditions

For the gas component, we use closed boundaries where the surface density and azimuthal velocity fields are scaled using the closest active cell, the radial velocity field is mirrored, and the energy field is extrapolated symmetrically. For the dust component, we use open/inflow boundary conditions. Like Sturm et al. (2020), we set the radial velocity at the boundaries to the radial drift velocity (an extrapolation based on Equations (23)–(26) of Takeuchi & Lin 2002):

$$v_{r,\text{dust}} = \frac{\eta v_{\text{Kep}}}{\text{St} + \text{St}^{-1}} \propto \left(\frac{H}{r}\right)^2 v_{\text{Kep}} \propto r^{2f-1/2}, \quad (11)$$

where v_{Kep} is the Keplerian velocity and $\eta = \left(\frac{H}{r}\right)^2 \frac{d \log(P)}{d \log(r)}$. These radial velocity boundary conditions are desirable for us because they negate the effect of radial drift accumulating over time, meaning we avoid any dust pileup at the inner boundary or depletion of dust in the outer disk that might impinge on the expression of the planet-driven spiral.

At the radial boundaries, we employ wave damping zones (de Val-Borro et al. 2006) to minimize wave reflections, where the damping zones’ inner and outer edges have a Keplerian orbital frequency ratio of 2/3 (Equations (A3) and (A4) of McNally et al. 2019). For our domain, the inner and outer edges of the damping regions work out to $0.131 r_p$ and $2.289 r_p$. We apply damping to each of the density, azimuthal, and radial velocity fields, with a local damping timescale of $1/(30 \Omega_{\text{Kep}}(r))$.

2.2. Radiative Transfer Calculations

Prior to any post-processing, we radially truncate the disk to extend from 0.2 – $2.2 r_p$ in order to remove the damped zones. We model our choice of physical disk parameters after the disks in the DSHARP survey, setting the stellar mass and

stellar luminosity to the median of the sample, $M_* = 0.8 M_\odot$ and $L_* = 1.5 L_\odot$ (Table 1 of Andrews et al. 2018), and the orbital radius of the planet to be roughly coincident with the radial location where many of the DSHARP gaps and rings are found, $a_p = 50$ au (Figure 7 of Huang et al. 2018a). The disk thus extends from 10–110 au. We place the disk at a distance of $d = 140$ pc and assume it has zero inclination (i.e., is face-on), giving the disk diameter (220 au) an angular size of $1.57''$.

A key point we emphasize in this work is that both the dust surface density and dust temperature contribute to the emergent dust intensity, I_ν , the observed quantity in ALMA continuum images. We calculate I_ν as

$$I_\nu = B_\nu(T_{\text{dust}}) \cdot (1 - e^{-\tau_\nu}), \quad (12)$$

where $B_\nu(T)$ is the Planck function, T_{dust} is the dust temperature, and τ_ν is the disk optical depth. Throughout, our observing frequency is $\nu = 345$ GHz. The dust temperature contributes via the first factor, $B_\nu(T_{\text{dust}})$, and the dust surface density via the second, $(1 - e^{-\tau_\nu})$.

In the first factor, $B_\nu(T_{\text{dust}})$, we use a different dust temperature distribution for each equation of state. For the adiabatic simulations, we convert the FARGO3D output (gas) energy field into temperature in units of Kelvin, and assume thermal equilibrium between gas and dust such that $T_{\text{dust,adi}} = T_{\text{gas}}$. We justify this assumption in Appendix B.

For the isothermal simulations (which do not solve the energy equation), we create an axisymmetric dust temperature map using Equation (B2) of Dong et al. (2018b):

$$T_{\text{dust,iso}} = 13.37 \left(\frac{r}{100 \text{ au}}\right)^{-1/2}, \quad (13)$$

which is the temperature profile consistent with disks heated by a central star of luminosity $L_* = 1.5 L_\odot$ and aspect ratio of Equation (7). At a radius of $a_p = 50$ au, Equation (13) yields a temperature of 18.9 K, a sound speed of 0.26 km s^{-1} , a physical scale height of 3.44 au and an aspect ratio just under 0.07 (hence our selection of $h_p = 0.07$ in Section 2.1). A physical disk may have a vertical temperature gradient (e.g., Rosotti et al. 2020), but (sub-)millimeter-sized grains are expected to settle to the disk midplane and adopt the temperature there.

In the second factor, $(1 - e^{-\tau_\nu})$, the disk optical depth is

$$\tau_\nu = \kappa_\nu \cdot \Sigma_{\text{dust}}, \quad (14)$$

where Σ_{dust} is the dust surface density output from FARGO3D and $\kappa_{345 \text{ GHz}} = 3.45 \text{ cm}^2 \text{ g}^{-1}$ (Beckwith et al. 1990).

We vary the disk optical depth by initializing the hydro simulations with a fixed dust-to-gas ratio of 0.01 and different Σ_0 (Equation (10)). The dust-to-gas ratio then evolves at each radii in the simulations. Throughout the paper, we use the term τ_0 to represent the optical depth at $\nu = 345$ GHz and $r = r_p$ at the beginning of our simulations, and we construct our simulation input parameters to give $\tau_0 = 0.1, 0.3, 1.0,$ and 3.0 . Of course, a particle of fixed grain size embedded in a higher density gas disk will be better coupled, and we account for this by setting up the initial dust Stokes number accordingly. For example, the dust in our $\tau_0 = 0.1$ disk has an initial Stokes number of $\text{St}(r_p) = 9 \times 10^{-3}$ via $\Sigma_0 = 2.89 \text{ g cm}^{-2}$, and the optically thickest $\tau_0 = 3.0$ disk has initial $\text{St}(r_p) = 3 \times 10^{-4}$ via $\Sigma_0 = 86.9 \text{ g cm}^{-2}$. For a reference comparison between the $\tau_0 = 0.1, 0.3, 1.0,$ and 3.0 disks,

Figure 12 in Appendix A provides radial profiles of Σ_{gas} , Σ_{dust} , St , T_{dust} , $\tau_{345 \text{ GHz}}$, and $I_{345 \text{ GHz}}$ for our adiabatic ($\beta = 10$) disk with a $1.0 M_{\text{th}}$ embedded planet.

2.3. Synthetic ALMA Observations

To explore ALMA’s capability to detect planet-driven dust spirals, we generate synthetic Band 7 continuum observations for a range of integration times and antenna configurations with the CASA software package (McMullin et al. 2007). Our choice of observing band strikes a balance between angular resolution (favoring shorter wavelengths), signal-to-noise ratio (S/N) (favoring longer wavelengths), feasibility (disfavoring Bands 8–10), and popularity (favoring Band 6 or 7).

We observe the disk with both a compact and extended 12 m array configuration to simultaneously achieve a high angular resolution and a large maximum recoverable scale. We choose the configuration pairs C43-4 + C43-7, C43-5 + C43-8, and C43-6 + C43-9 following the Cycle 8 Proposer’s Guides. The maximum recoverable scales of the compact configurations C43-4, C43-5, and C43-6 are $\theta_{\text{MRS}} = 3''.3$, $1''.9$, and $1''.2$, respectively, so the C43-6 configuration does not quite cover emission on the angular scale of the disk, $\theta_{\text{LAS}} = 1.57''$. Observing with a compact configuration in addition to an extended one requires 20%–22% more on-source time, but we found that doing so improves uv sampling, reducing long baseline artifacts that exist with the high angular resolution configurations, giving the combined image overall higher quality; see Figure 16 in Appendix E for an illustration.

We set up the integration time to target a requested continuum sensitivity of 10, 15, 20, 25, 30, and $35 \mu\text{Jy} \text{bm}^{-1}$. As per the Sensitivity Calculator in the ALMA Cycle 8 OT, these requested sensitivities correspond to a combined on-source time (i.e., summed compact and extended configuration on-source time) of roughly 8.0 hr, 3.5 hr, 2.0 hr, 1.3 hr, 55 minutes, and 40 minutes, depending on the configuration pair. Table 1 in Appendix E provides the individual and combined on-source times, as well as the total time including overheads, for each requested sensitivity and antenna configuration pair.

We generate measurement sets for the compact and extended configurations using the `simobserve` tool. The disk is assumed to have R.A. and decl. J2000 $19^{\text{h}}00^{\text{m}}00.40^{\text{s}}00^{\text{m}}00$. We set the continuum bandwidth at 345 GHz to the full available 7.5 GHz, and adopt the default choices of a precipitable water vapor level of 0.913 mm and ambient ground temperature of 269 K. We concatenate the measurement sets from both configurations for each model and clean them simultaneously with `tclean`, and then generate the noisy images with `simanalyze`. CLEAN images are created using a Briggs weighting and a robust factor of 0.5. We clean to a threshold of three times the requested sensitivity. After cleaning, the measured rms noise in all our images presented in Section 4 is $\sim 80\%$ – 95% of the requested sensitivity (with cleaning affecting those images with poorer uv coverage more greatly).

3. Important Physics for the Observability of Planet-driven Dust Spirals

We employ two different metrics to quantify the characteristics of planet-driven spirals: (1) *perturbation*, and (2) *contrast*. We calculate the perturbation in X disk quantity

relative to an unperturbed disk as

$$\delta X / X_{\text{no planet}} \equiv (X - X_{\text{no planet}}) / X_{\text{no planet}}, \quad (15)$$

where $X_{\text{no planet}}$ is the state of an identical *no planet* simulation,⁵ at the same time snapshot. Our definition of perturbation is motivated from a theoretical perspective as it isolates the effect of the planet. Contrast is defined relative to the azimuthal average of the perturbed disk as

$$\text{contrast in } X \equiv (X - \bar{X}_{\phi}) / \bar{X}_{\phi}, \quad (16)$$

where \bar{X}_{ϕ} is the azimuthal average of the same disk, again at the same time. Our definition of contrast is motivated from an observational perspective, as an observer only has one disk to work with.

The hydrodynamic models presented in Figures 2 and 3 of this section are our shorter (15 orbits) set, described at the end of Section 2.1, which we conducted with a $M_{\text{p}} = 1.0 M_{\text{th}}$ planet and without a planet; Figure 4 uses our radiative transfer models (1500 orbits).

3.1. Do Dust Spirals Look Different from Gas Spirals?

When a dust particle encounters the spiral wave, it experiences a temporary additional drag force due to the gas velocity perturbation and is disturbed from its near-Keplerian orbit. The degree of dust-gas coupling will determine the morphology of the resulting dust spiral. Throughout this paper, we use the term *well coupled* to describe dust that forms spirals morphologically identical their gas spiral counterparts, and *poorly coupled* to refer to dust whose spirals are morphologically different. In this section we investigate the morphology of well-coupled and poorly coupled dust spirals, and pinpoint the Stokes number that divides the two regimes.

Location of spiral peaks. In Figure 2(a), we trace the peaks of the spiral surface density perturbations (Equation (15)) in the gas and two species of dust, $St = 4 \times 10^{-1}$ and $St = 10^{-2}$. In comparing them to the gas, we see that these two species represent examples of poorly coupled and well-coupled dust, respectively. The spine of the well-coupled dust spiral overlaps with that of the gas spiral perfectly throughout the disk. On the other hand, the poorly coupled dust spiral lags behind the gas; the azimuthal offset between the two at $r = 1.7 r_{\text{p}}$ for example is $20^{\circ}.04$.

Spiral amplitude. In Figure 2(b), we show an azimuthal cross section of the spiral surface density perturbation in the gas and five species of dust—two Stokes numbers representative of well-coupled dust ($St = 10^{-3}$, 10^{-2}), one marginal ($St = 10^{-1}$), and two poorly coupled ($St = 4 \times 10^{-1}$, 1). In addition to lagging behind the gas, the poorly coupled dust spiral peaks are lower in amplitude. In contrast, the well-coupled dust spirals are indistinguishable from the gas. The marginal case suggests the decoupling boundary occurs between $St = 10^{-2}$ and 10^{-1} .

What is well-coupled dust in the context of planet-driven spirals? We can estimate the Stokes number that divides the well-coupled and poorly coupled regimes with a timescale argument, first described by Sturm et al. (2020), where we compare the time it takes a dust particle to cross the gas spiral wake to the particle’s intrinsic stopping time. First, we define $\Delta\phi_{\text{gas spiral}}$ to be the azimuthal width of the gas spiral as a

⁵ Sturm et al. (2020) also use an empty simulation as the unperturbed disk (private communication), but use notation X_0 instead of $X_{\text{no planet}}$. Normalizing with an empty simulation instead of the initial state is an easy way to account for radial drift-induced perturbations in the dust.

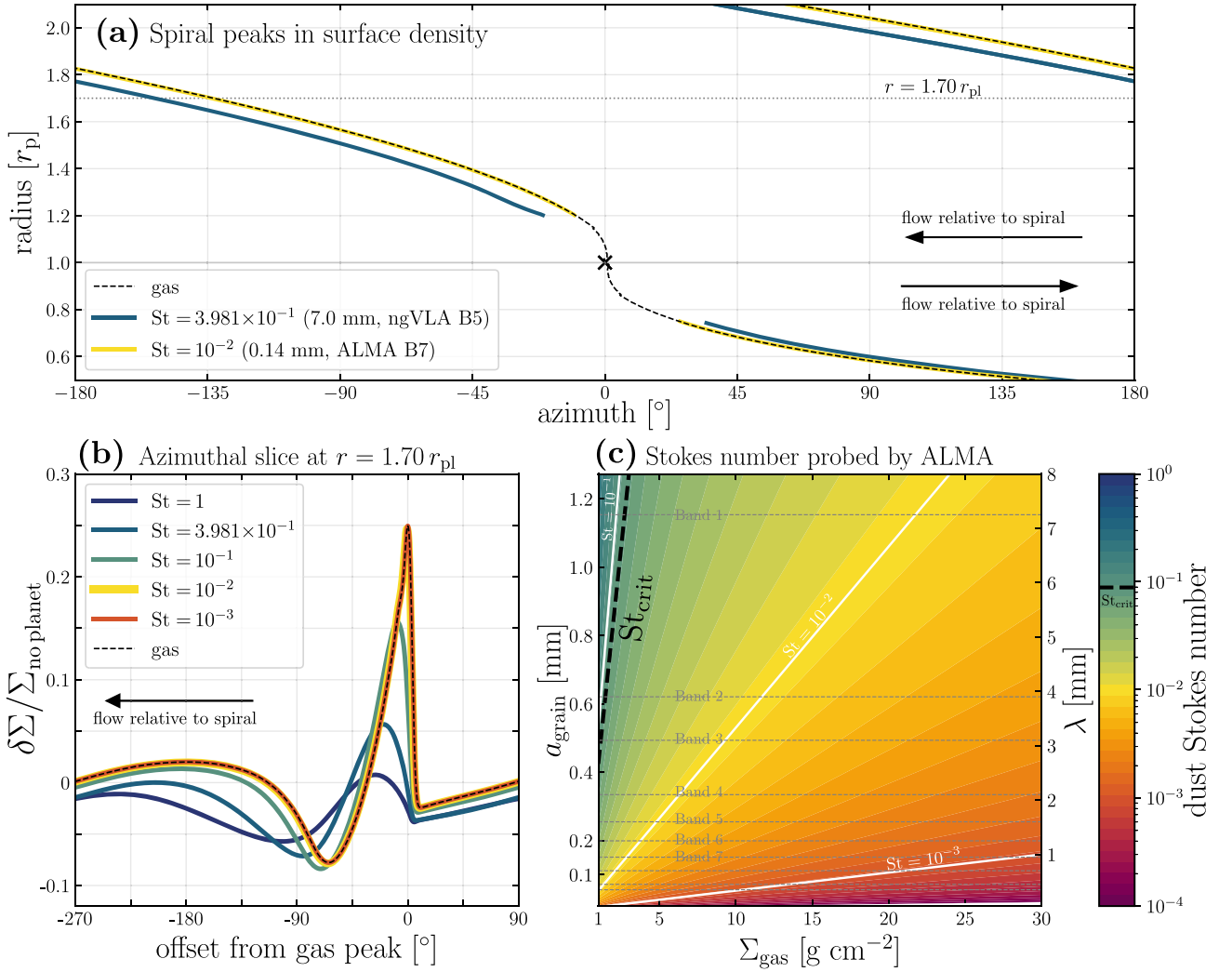


Figure 2. Spiral morphology in surface density, and expectations for ALMA observations. (a) The spine of the inner and outer primary spiral arm in the gas, one species of well-coupled dust ($St = 10^{-2}$, or $a_{\text{grain}} = 0.14$ mm if $\Sigma_{\text{gas}} = 3$ g cm $^{-2}$) and one of poorly coupled dust ($St = 0.4$, 7.0 mm), driven by a $1.0 M_{\text{th}}$ planet in an adiabatic ($\beta = 10$) disk. Poorly coupled dust ($St > St_{\text{crit}} = 0.089$, Equation (18)) forms spirals whose peaks azimuthally lag behind the gas. (b) An azimuthal slice of the surface density perturbation far from the planet ($r = 1.7 r_{\text{pl}}$), for gas and 5 species of dust (two well coupled, one marginal, two poorly coupled). In addition to being azimuthally offset, $St > St_{\text{crit}}$ dust spirals have smaller amplitude. Note the yellow $St = 10^{-2}$ curve has been made 2 pts thicker to be visible behind the red $St = 10^{-3}$ curve. (c) Stokes number calculated for a range of gas surface densities and ALMA dust grain sizes. For typical observing wavelengths of each ALMA band, we mark the dust grain size probed assuming (LH y-axis) $a_{\text{grain}} = \lambda_{\text{obs}}/2\pi$ (RH y-axis). In general, ALMA probes well-coupled dust spirals.

fraction of a full revolution, measuring it as the FWHM⁶ in the perturbed surface density (i.e., the *foot* is at $\delta\Sigma/\Sigma_{\text{no planet}} = 0$ in the gas). Note that $\Delta\phi_{\text{gas spiral}}$ is a function of, at a minimum, planet mass and radius. With that number, we calculate the gas spiral crossing time (Equation (5) of Sturm et al. 2020):

$$t_{\text{cross}} = \Delta\phi_{\text{gas spiral}} \frac{t_{\text{dyn}}}{(1 - \Omega_{\text{p}} t_{\text{dyn}})}, \quad (17)$$

where $t_{\text{dyn}} = 1/\Omega_{\text{Kep}}$ is the dynamical time and Ω_{p} is the planet's (and therefore the gas spiral's) angular velocity. This equation assumes the dust moves at Keplerian velocity, and takes into account the additional time a particle spends in the spiral because the spiral moves in the same direction as the Keplerian flow.

Following Sturm et al. (2020) we define the *critical* Stokes number—the boundary between what constitutes well-coupled and poorly coupled dust—as the Stokes number for which t_{cross}

and t_{stop} (Equation (9)) are equal:

$$St_{\text{crit}} \equiv \frac{\Delta\phi_{\text{gasspiral}}}{(1 - \Omega_{\text{p}} t_{\text{dyn}})}. \quad (18)$$

For the disk and planet parameters of Figure 2, we find $\Delta\phi_{\text{gas spiral}} = 0.05$ and $St_{\text{crit}} = 0.089$ at $r = 1.7 r_{\text{pl}}$, in agreement with the results presented in the top and bottom left panels. The critical Stokes number offers an intuitive picture: Dust with Stokes number higher than St_{crit} takes longer to respond to the gas spiral drag forces than the amount of time those forces act on them, and so their spiral morphology is different.

What are the implications for ALMA observations? In Figure 2(c), we calculate the dust Stokes number for a range of gas surface densities Σ_{gas} and dust sizes a_{grain} (Equation (9)). The horizontal lines mark the ALMA bands at which dust of a certain size is probed the best, assuming the median observing wavelength at each band $\lambda_{\text{obs}} = 2\pi a_{\text{grain}}$ (Equation (8)).

⁶ In contrast to Sturm et al. (2020), who estimate it using a Gaussian fit.

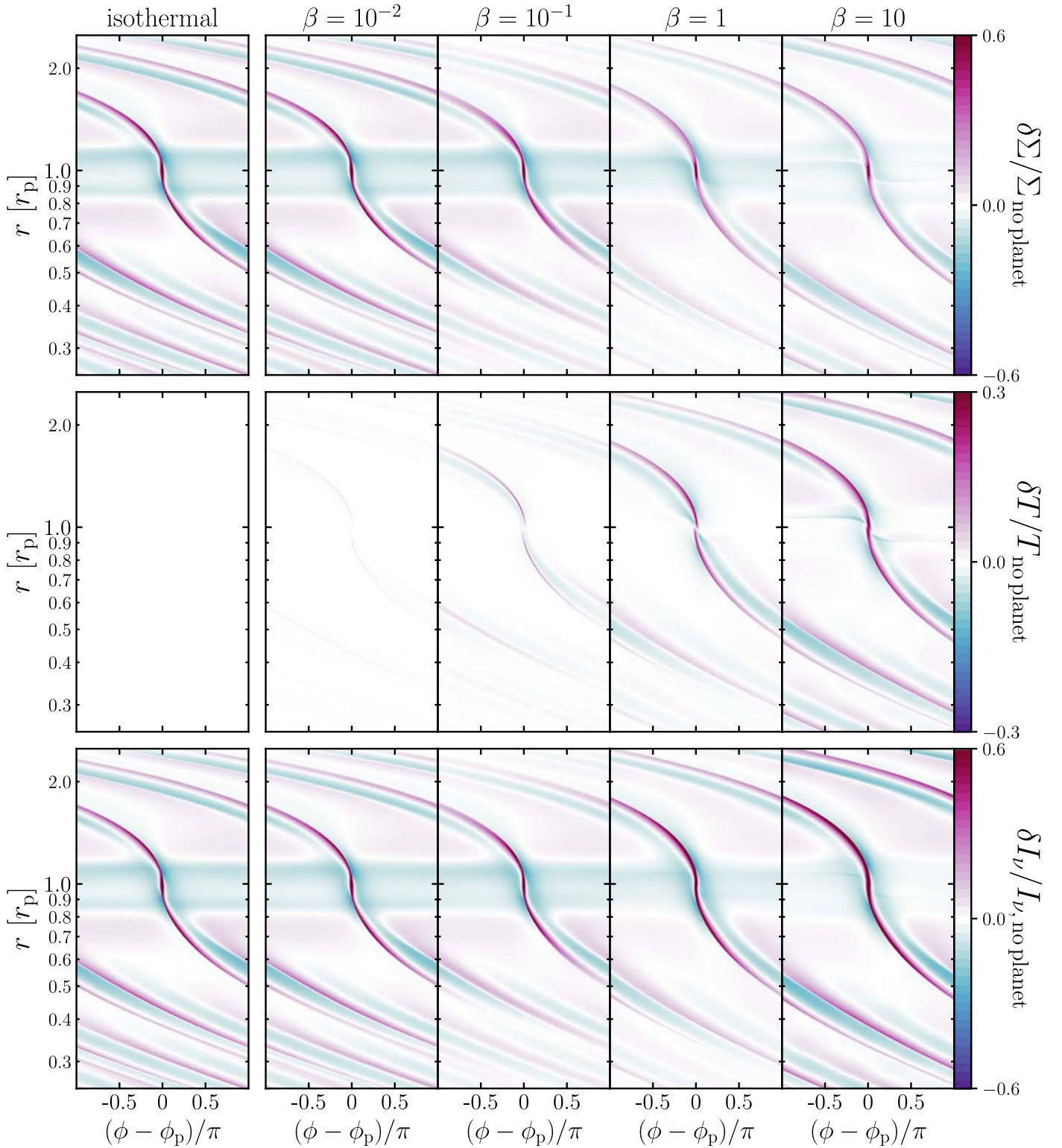


Figure 3. Planet-induced spiral perturbations (Equation (15)) in disks with increasing cooling timescales β (left to right). The spiral dust surface density perturbation (top) is largest in isothermal disks, whereas the temperature perturbation (middle) is necessarily zero in isothermal disks and increases monotonically with the cooling time. As a result, the observable dust intensity perturbation (bottom), shown here in the optically thin limit ($I_\nu \propto \Sigma_{\text{dust}} B_\nu(T_{\text{dust}})$, where $\nu = 345$ GHz), is largest in adiabatic disks that cool slowly. See also Figure 13 in Appendix C. The planet mass is $M_p = 1.0 M_{\text{th}}$. Note that the color bar range in the temperature row is half the value in the other two rows.

$St_{\text{crit}} = 0.089$ (dashed black line) delineates the well-coupled and poorly coupled regimes. This panel shows that, at almost all observing wavelengths and gas surface densities, ALMA

probes well-coupled dust ($St < St_{\text{crit}}$). We therefore expect that planet-driven dust spirals observed by ALMA will be perfect tracers of their parent gas spirals at the disk midplane.

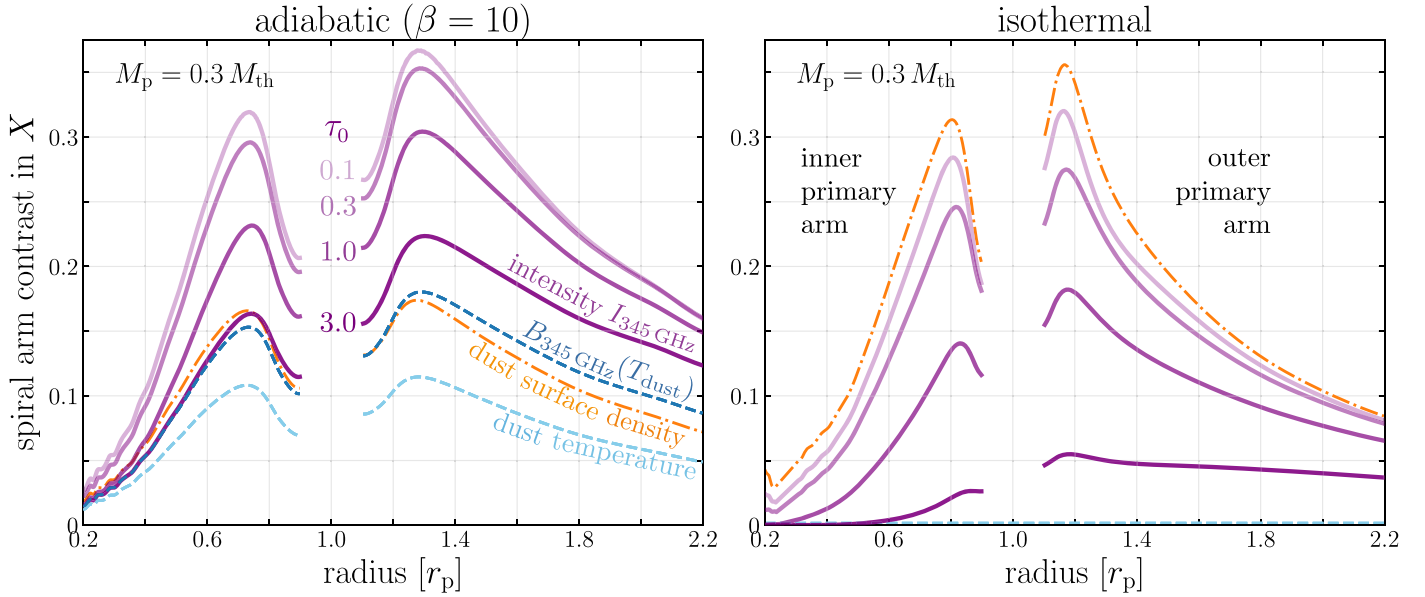


Figure 4. Spiral arm contrast (Equation (16)) in dust surface density (orange dotted–dashed), temperature (light blue dashed), $B_{345 \text{ GHz}}(T_{\text{dust}})$ (dark blue dashed) and intensity (shades of solid purple) traced along the inner and outer primary arms induced by a $0.3 M_{\text{th}}$ planet. The shades of purple distinguish the dust intensity at different disk optical depths, from light (optically thin) to dark (optically thick); τ_0 is the initial optical depth at r_p . The dust surface density spiral contrast in the isothermal case (right) is higher than that in the adiabatic one (left), but the former represents the upper bound of an isothermal spiral’s contrast in intensity. Due to the presence of a temperature spiral in the adiabatic disks, the adiabatic spiral intensity contrast can exceed its dust surface density contrast and be brighter than in isothermal disks—particularly at high τ .

3.2. The Ingredients of Intensity: In What Disks are Dust Spirals Most Prominent?

Both the surface density of the dust and its temperature contribute to the overall dust thermal emission that we detect with ALMA continuum observations. It is therefore relevant for the observability of planet-driven dust spirals to understand how the spirals manifest in both the dust surface density and temperature, and to disentangle each ingredient’s contribution to the surface brightness of the spiral.

From top to bottom, Figure 3 shows the perturbations (Equation (15)) in dust surface density, dust temperature, and the resultant dust intensity in the optically thin limit generated by a $1.0 M_{\text{th}}$ planet. As we are interested in ALMA observations, we focus on well-coupled dust ($\text{St} \ll \text{St}_{\text{crit}}$; Section 3.1). From left to right, we show these quantities in a locally isothermal disk and in disks with an adiabatic equation of state and different dimensionless cooling timescales. The dependence of these three perturbation quantities on the cooling rate is not always monotonic, and the five selected cases ($\beta = 10^{-2}$, 10^{-1} , 1, 10 and the isothermal equation of state representing the limit $\beta \rightarrow 0$) represent the full range of behaviors for the thermodynamics we consider. Complementing this figure is Figure 13 in Appendix C.

Dust surface density. Consider first the surface density perturbation, shown in the top row of Figure 3. In the entire domain, the density spiral amplitude is strongest in the locally isothermal disk, while it drops by $\lesssim 10\%$ when β increases to 10^{-2} . At the other extreme, the density spiral amplitude in disks with $\beta \geq 10$ are $\sim 50\%$ as strong as the isothermal case near the planet ($0.6 r_p < r < 2.0 r_p$) but become more comparable further away. In the intermediate cases, $10^{-1} \leq \beta \leq 1$, the spiral density waves also start $\sim 50\%$ as strong as the isothermal case near the planet, but are significantly damped as they propagate. These results agree with those presented in Miranda & Rafikov (2020b, their Figure 1) and Zhang & Zhu (2020, their Figure 1); efficient cooling leads to stronger

compression. If we considered the well-coupled dust surface density alone, we might naively expect spirals to have higher contrasts, and thus be easier to detect given the same background disk surface brightness, in disks with short cooling timescales.

Dust temperature. In the middle row of Figure 3, we present the temperature perturbation. It is the strongest near the planet and decreases as the waves propagate in both directions. Here, the dependence on the cooling timescale is monotonic—the temperature spiral amplitude at all radii is an increasing function of β , as inefficient cooling results in larger temperature increase from adiabatic compression. The results are in agreement with Muley et al. (2021).

Dust intensity. The bottom row of Figure 3 shows the intensity perturbation in the optically thin limit, i.e., $I_{345 \text{ GHz}} \propto \Sigma_{\text{dust}} B_{345 \text{ GHz}}(T_{\text{dust}})$. In this way we demonstrate the effect of the temperature spiral without the added complication of disk optical depth, as a start. The surface density and temperature perturbations combine to give the intensity spiral amplitude a non-monotonic dependence on the dimensionless cooling timescale. It is largest in adiabatic disks with $\beta \geq 10$ at all disk radii. In other words, dust spirals are more prominent in slow cooling disks. The inner and outer primary spiral amplitude in the $\beta = 10$ case is uniformly $\sim 20\%$ higher than in the locally isothermal disk (Figure 13 in Appendix C).

A second crucial effect of the temperature spiral—or more fundamentally, the dimensionless cooling timescale—is to introduce a degeneracy between the intensity spiral amplitude and the planet mass. Comparing the two most different cases, the intensity perturbation amplitude at $r = 1.7 r_p$ is 0.13 for $\beta = 10^{-1}$ and 0.45 for $\beta = 10$. This is a factor of 3.5 different for the same $1.0 M_{\text{th}}$ planet.⁷

⁷ Fixing instead the cooling timescale to $\beta = 10$ and varying the planet mass by a factor of 10 (from 0.3 – $3.0 M_{\text{th}}$), the amplitude difference is a factor of 2.4.

In Figure 4 we bring back the complication of disk optical depth by using the results of our radiative transfer calculations, and switch to our observationally motivated metric to quantify the spiral, the *contrast* (Equation (16)). Figure 4 shows the contrast traced along the inner and outer primary spiral arms in dust surface density, temperature, and intensity, where intensity has now been calculated with the radiative transfer equation (Equation (12)) for a range of disk optical depths. As per the first factor of Equation (12), we also plot the contrast in $B_{345\text{ GHz}}(T_{\text{dust}})$. The driving planet has a mass $M_p = 0.3 M_{\text{th}}$. We show the results for the locally isothermal disk and compare them to a disk with an adiabatic equation of state and $\beta = 10$.

Comparing the spiral surface density contrast between the two disks first, we see again that the isothermal case exhibits the most prominent density spirals. The difference is most significant (roughly a factor of 2) close to the planet (within $0.4 r_p$ on either side). However, the spiral density contrast in the isothermal case constitutes an upper bound for how *bright* spirals can be in that disk. For any nonzero optical depth, the isothermal spiral intensity contrast is lower than its dust density contrast.

In adiabatic disks on the other hand, the spiral intensity contrast can be larger than the density contrast, depending on the significance of the temperature spiral. In the $\beta = 10$ case, the spiral temperature contrast is $\sim 70\%$ as strong as the density contrast, and is enhanced by the Planck function to give a contrast in $B_{345\text{ GHz}}(T_{\text{dust}})$ that is $\sim 110\%$ as strong. This results in a spiral intensity contrast that not only exceeds its own density contrast, but that is also larger than the intensity contrast in the locally isothermal disk.

This difference between spirals in isothermal and adiabatic disks becomes more pronounced when the disk is optically thick. For an initial optical depth at the planet’s orbital radius of $\tau_0 = 3.0$, the spiral intensity contrast in the adiabatic $\beta = 10$ disk is 3–4 times larger than in the isothermal disk. The temperature spiral in adiabatic disks represents a *floor* for the spiral intensity; as τ increases it takes on a greater fraction of the responsibility for making adiabatic spirals brighter than isothermal ones, while isothermal spiral contrast disappears when $\tau \rightarrow \infty$.

Finally, we note that the outer spiral arm can have 10%–40% larger contrast in intensity than the inner arm at its peak at various optical depths. This, combined with that the outer spiral fades more slowly as it propagates away from the planet, makes the outer spiral easier to identify in observations.

4. Synthetic ALMA Observations: An Observer’s Guide

In this section, we present synthetic ALMA B7 continuum observations and our method of highlighting the planet-driven spiral signal. We report trends in the amount of ALMA time needed under different disk and observing conditions (Section 4.1); we describe the impact of different ALMA antenna configurations (Section 4.2); we feature a successful recovery of the spiral driven by a low mass planet (Section 4.3); and we show the impact that gaps and rings could have on our ability to recognize colocated spiral arms (Section 4.4).

In Figure 5 we show a gallery of 16 synthetic ALMA continuum images, a representative selection from our full set,⁸

⁸ The results from our full set ($\times 3$ planet masses, $\times 4$ disk optical thicknesses, $\times 2$ equations of state, $\times 3$ antenna configuration pairs, $\times 6$ integration times = 432 model images and their residual maps) are available at FigShare: [10.6084/m9.figshare.19148912](https://figshare.com/10.6084/m9.figshare.19148912).

obtained with the C43-5 + C43-8 configuration pair (beam size 31×35 mas). This gallery demonstrates the outcomes under a variety of disk and observing conditions: two integration times (8 hr versus 40 minutes on source), two equations of state (adiabatic with a cooling timescale $\beta = 10$ versus isothermal), two disk optical depths (marginally optically thin $\tau_0 = 0.3$ versus optically thick $\tau_0 = 3.0$), and two planet masses ($M_p = 1.0$ or $3.0 M_{\text{th}}$). In panels (e)–(h) and (p), the outer primary spiral arm is very clearly visible in the continuum image. In panels (f) and (h), the inner primary (and panel (h), the inner secondary) arm can also be seen. We have labeled the outer primary (OP), inner primary (IP), and inner secondary (IS) arms in panel (h).

In order to quantify the robustness of these detections, and in order to amplify the spiral signal in less conspicuous cases, we make residual maps for all our synthetic observations—in the image plane. We first transform the ALMA image in on-sky coordinates into polar (r, ϕ) coordinates,⁹ then average the observed intensity over the full azimuth to obtain an axisymmetric disk, $\overline{I_{\text{obs}} \phi}$. We subtract that map from the observed image and normalize the difference by the observation’s rms noise, such that the reported quantity in residual maps is $S/N = (I_{\text{obs}} - \overline{I_{\text{obs}} \phi}) / (\text{rms noise})$. Figure 6 presents such residual maps for the observations in Figure 5.

The strongest dust spiral recovery in all our permutations of disk conditions is the one in panel (h) of Figures 5 and 6: a $3.0 M_{\text{th}}$ planet in an adiabatic ($\beta = 10$), optically thick ($\tau_0 = 3.0$) disk. Change the disk’s equation of state to locally isothermal (panel (d)), and the spiral hardly appears in the residuals at all. Decreasing the planet mass to $1.0 M_{\text{th}}$ (panel (f)) decreases the spiral S/N, but it is still strong. Decrease the disk optical depth by a factor of 10 (panel (g)) and some parts of the inner primary arm are lost, but three spiral arms (outer primary, inner primary, inner secondary) are still visible in the residuals. The outer spiral driven by the planet in panel (h) is so significant that it is identifiable in the residuals of a 40 minute observation (panel (p)).

From Figure 5 we conclude that the signal from planet-driven dust spirals in isothermal disks is very weak in comparison to those in adiabatic disks that cool slowly. We also see that even though spiral intensity contrasts are intrinsically larger in optically thin disks (Figure 4), they are actually more difficult to observe due to the disk being dimmer overall.

Before moving on to permutations of observing conditions, a few remarks on residual maps. First, we find that they are an excellent tool for probing spirals, though this comes with the caveat that they are easy to make for our face-on model disks and may not be as straightforward to make for real disk observations. Second, we emphasize the importance of plotting both the positive *and negative* residuals when searching for planet-driven spirals. Detecting both a spiral’s peak and its associated trough can lend weight to the detection of the structure, as well as to the conclusion that it is companion driven because they are predicted together by density wave theory (e.g., Bae & Zhu 2018a). We also tried making residual maps in the visibility plane using `frankenstein` (Jennings et al. 2020), which has been shown to produce accurate fits to real visibility data (e.g., Jennings et al. 2022), but with our

⁹ We use the `polarTransform` python module: <https://polartransform.readthedocs.io/en/latest/>.

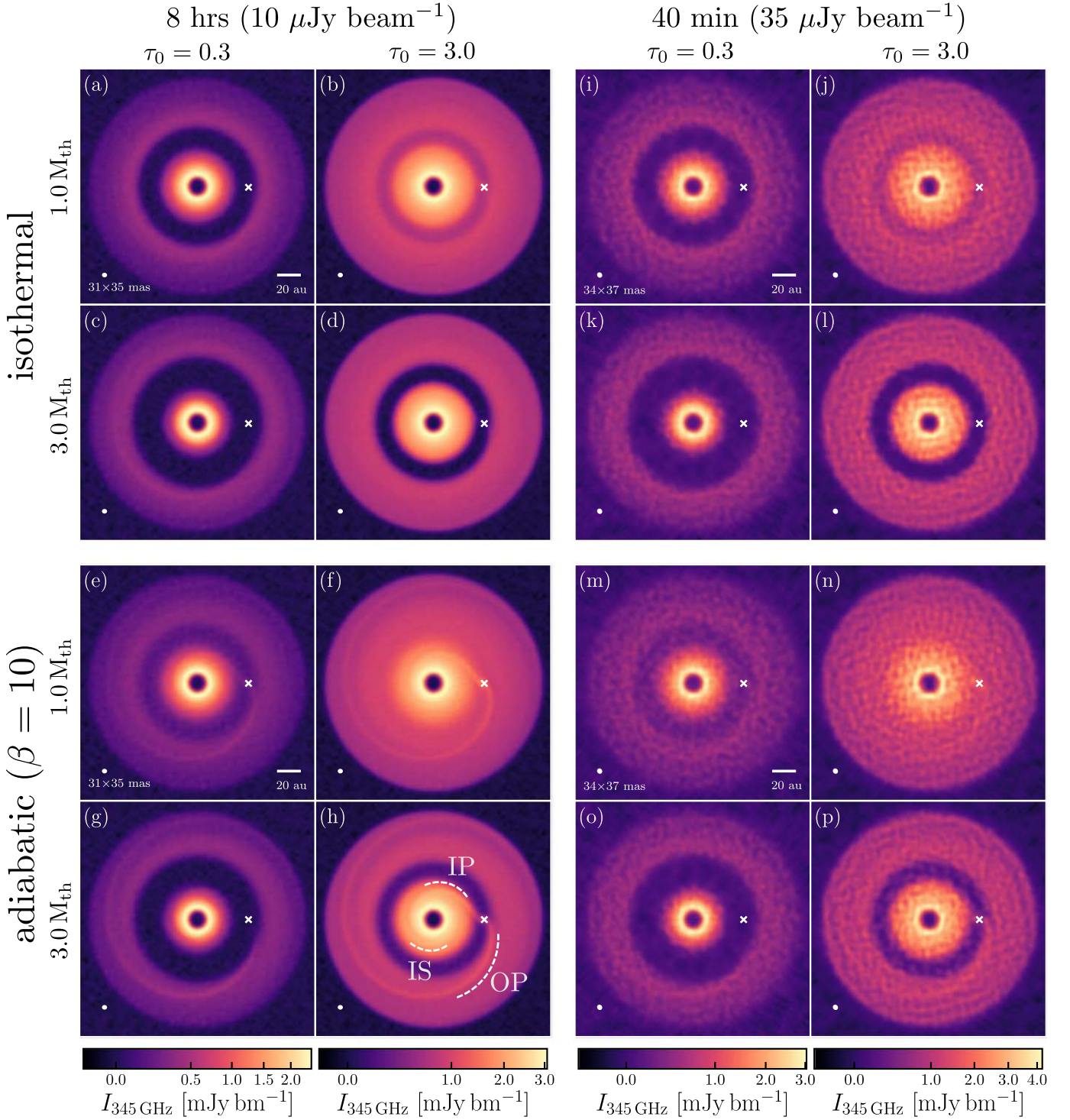


Figure 5. A selection of synthetic ALMA B7 continuum images with the C43-5 + C43-8 configuration pair, demonstrating trends with equation of state (top vs. bottom), combined on-source time (left vs. right), planet mass (inner top versus inner bottom), and disk optical depth (inner left vs. inner right). The requested sensitivity (number in brackets, e.g., $10 \mu\text{Jy beam}^{-1}$) is what was used to determine the combined on-source time (e.g., 8 hr). The synthesized beam is shown in the bottom left corner of each image, and each color bar applies to the whole column. Images are shown with a 1/2-power-law stretch. The full set of images is available at FigShare: [10.6084/m9.figshare.19148912](https://figshare.com/10.6084/m9.figshare.19148912).

models we found that the imaged frank visibility residuals showed the spiral less clearly (see Figure 15 in Appendix E).

4.1. How Much ALMA Time Do You Need?

It is a priori possible that observing planet-driven spirals requires very deep observations. To test this possibility, we

created ALMA observations achieving requested sensitivities of 10, 15, 20, 25, 30, and $35 \mu\text{Jy beam}^{-1}$ with 8.0, 3.5, 2.0, 1.3, 0.9, and 0.7 hr of combined on-source time (totaling roughly 20, 9.0, 5.0, 3.8, 2.5, and 2.0 hr with overheads) and judged whether the spiral was detected in each case. For context, the DSHARP program had a median integration time of ~ 1.4 hr

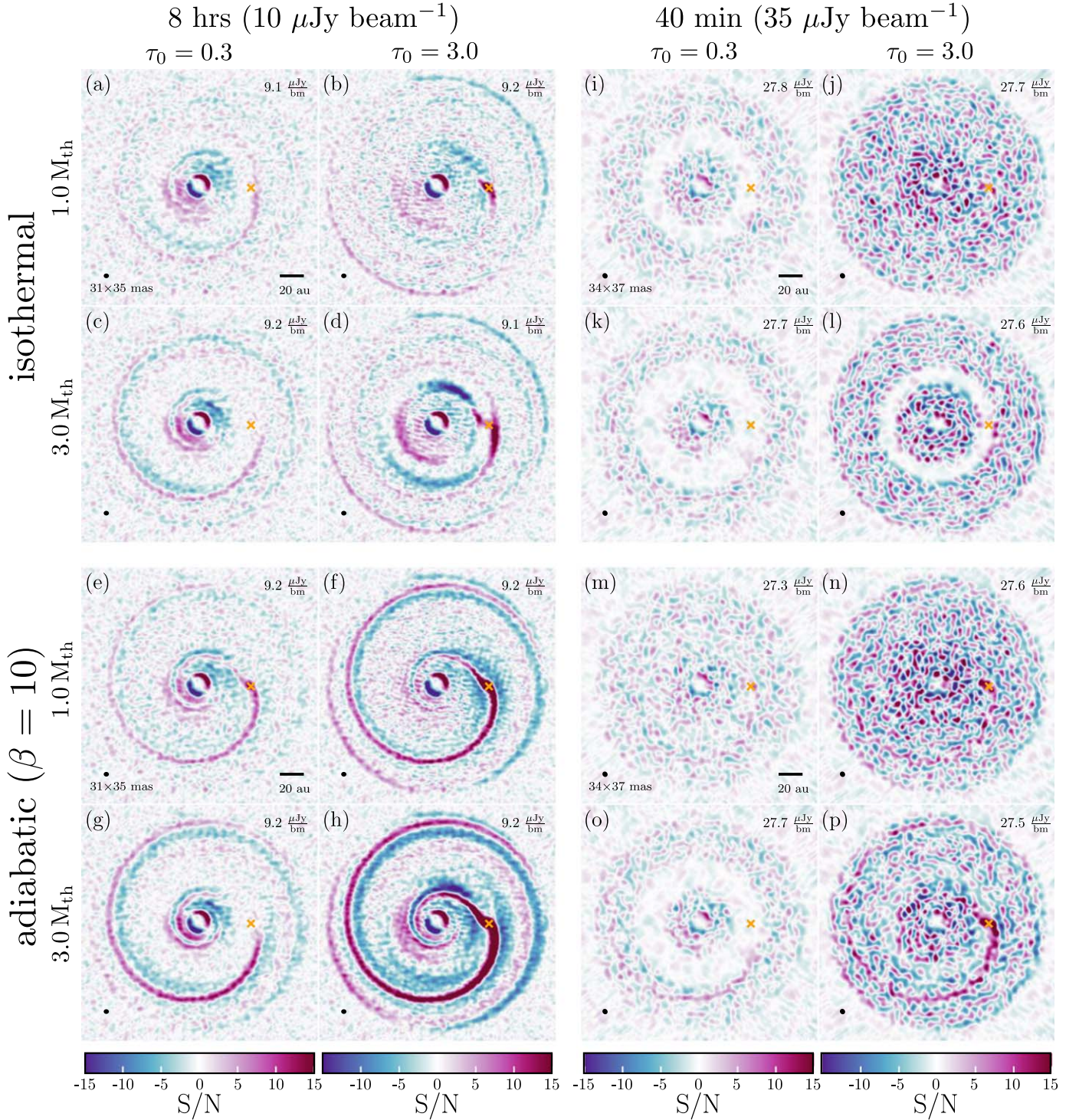


Figure 6. Residual maps of the observations in Figure 5. The S/N is calculated as $S/N = (I_{\text{obs}} - \overline{I_{\text{obs},\phi}}) / (\text{rms noise})$, where $\overline{I_{\text{obs},\phi}}$ is an axisymmetric disk obtained by azimuthally averaging in the image plane. The measured rms noise in each observation after cleaning is written in the top right corner of each panel, and in all cases is $\sim 10\%$ – 20% less than the requested sensitivity.

(Andrews et al. 2018), and the longest integration done on a single disk to date (achieving a sensitivity and beam size comparable to our models, $25.7 \mu\text{Jy beam}^{-1}$ and $\theta_{\text{AR}} = 24.6 \text{ mas}$ in B7) is 5.59 hr of on-source time toward HL Tau (2019.1.01051.S, currently in progress). Our maximum

on-source time thus pushes the envelope by ~ 2.5 additional on-source hours.

To decide on a criterion for successful spiral recovery, we considered: *how does one recognize a spiral?* By definition, a spiral is a structure that extends some range in azimuth $\Delta\phi$ for

each increment in radius Δr . The more azimuth $\Delta\phi$ we notice the structure spanning, the more confident we are that it is a spiral and not a segment of a circle, or an azimuthal asymmetry. Motivated by that concept, we set the criterion for a successful spiral recovery to be that we can trace the outer spiral arm in our residual maps with $S/N=5$ contours over at least 90° continuously in azimuth (not necessarily starting from the known planet location). We chose to focus on the outer primary spiral because it has a larger intrinsic contrast (Figure 4) and was more often apparent in our residual maps (Figure 6) than the inner primary arm. Structures at larger radii also naturally have larger angular extent.

Figure 7 is a visual table depicting the amount of on-source time required to recover the outer spiral arm under our 72 permutations of disk and observing conditions ($\times 2$ EoS $\times 3 M_p \times 4 \tau_0 \times 3$ configuration pairs). We created this figure by identifying, for each permutation, the observation with the least on-source time that still recovered the spiral. That minimum on-source time is colored by the corresponding ALMA OT requested sensitivity. White space (with gray text, e.g., >8.1 hr) indicates that we were not able to recover the spiral under those disk and observing conditions with our maximum tried on-source time.

Figure 7 shows that, if they are present, planet-driven dust spirals are easier to observe (i.e., require less integration time to detect) in adiabatic disks that cool slowly ($\beta \gtrsim 10$), that are marginally but not too optically thick ($\tau_0 \gtrsim 1.0$), and that host massive planets ($M_p \gtrsim 1.0 M_{\text{th}}$). In such disks, spirals can be detected with integration times on the order of hours.

4.2. What Angular Resolution Do You Need?

Planet-driven spiral arms are intrinsically fine structures with widths comparable to scale height (e.g., Figure 3). As such, it is natural to think that high angular resolution observations—observations that *resolve* the spiral—are necessary in order to detect them. We find that the situation is more nuanced, and that high resolution does not necessarily lead to best detectability.

In Figure 8, we show ALMA continuum observations and residual maps obtained with three different antenna configuration pairs: C43-4 + C43-7 ($\theta_{\text{AR}} = 0''.061$), C43-5 + C43-8 ($\theta_{\text{AR}} = 0''.028$), and C43-6 + C43-9 ($\theta_{\text{AR}} = 0''.017$), translating to 8.5, 3.9, and 1.7 au at $d = 140$ pc, respectively. We achieve a measured sensitivity of $\sim 13\text{--}15$ Jy bm^{-1} with ~ 3.5 hr of on-source time in all cases. The disk is adiabatic ($\beta = 10$), marginally optically thick ($\tau_0 = 1.0$) and contains a $1.0 M_{\text{th}}$ planet. If we approximate the spatial width of the spiral as $H(r_p) = 3.5$ au, we can see that the C43-7 configuration does not resolve the spiral, C43-8 is marginal, and C43-9 resolves the spiral with ~ 2 beams.

In the continuum images (top panels of Figure 8), we find the intuitive result: the spiral signal is *washed out* in the lower angular resolution observation (left panel). In the higher angular resolution image (right panel), the outer spiral is easily seen directly in the image, and even the inner spiral arm is visible. The explanation is simply that what is captured by a smaller beam can be comprised of a greater proportion of spiral signal than background disk signal, in comparison to the proportion captured by a larger beam. In other words, when the spiral is not fully resolved, a higher angular resolution observation has a higher spiral-signal-to-background ratio.

The nuance is introduced when one considers the *robustness* of the spiral detection, i.e., the spiral S/N . In the residual maps (bottom panels of Figure 8), we find that the lower angular

resolution observation with C43-4 + C43-7 detects the spiral with the highest S/N : we can trace $S/N=5$ contours over $\sim 270^\circ$, and $S/N=10$ contours over $\sim 90^\circ$. On the other hand, the detection with the higher angular resolution observation (C43-6 + C43-9) is less robust; it did satisfy our recovery criterion (Figure 7), but only just.

The explanation for this rests on two factors: (1) the observed intensity is in units of Jy bm^{-1} , not Jy arcsec^{-2} ; and (2) the observations we are comparing have very similar levels of rms noise. The spiral signal in Jy bm^{-1} is larger for a larger beam (due to the beam's larger *area*). Therefore, if noise is independent of beam size, the low angular resolution detection has a higher spiral S/N . This holds at all sensitivities that we explored. Of course, there is a minimum angular resolution required for spiral detection; one would need to resolve the distance between the spirals (think: Rayleigh criterion), and ideally any background structures on scales larger than the spiral.

The utility of archival or future continuum observations of real disks done at high angular resolution could be enhanced by uv tapering to produce larger beam sizes, possibly improving the S/N and helping identify the spiral signal in S/N space.

4.3. Detecting Spirals from Low Mass Planets?

Detecting a low mass planet embedded in a protoplanetary disk is an exciting prospect because if we believe planets grow in mass over some nonzero formation timescale, then *low mass* translates to early stage, and probing lower mass planets probes closer to their birth. The challenge is linearly proportional to the reward, however, because the amplitude of planet-driven spirals (in the sub-thermal mass regime) is proportional to the planet mass (Dong et al. 2011b; Bae & Zhu 2018a; Miranda & Rafikov 2019a). We observe many dust gaps and rings, which we believe could be the birth sites of planets, but as yet few colocated spirals. One possible explanation for the dearth of observed planet-driven spirals despite the abundance of observed gaps and rings could simply be that the spiral amplitude is too insignificant to be detected with ALMA. What is the lowest planet mass that drives a detectable dust spiral?

In Figure 9, we show a successful recovery of the outer spiral driven by our lowest mass planet, $0.3 M_{\text{th}}$ ($0.1 M_{\text{Jup}}$ or $1.6 M_{\text{Nep}}$, $q = 1.03 \times 10^{-4}$). As shown in Figure 7, if the disk is adiabatic and cools slowly ($\beta = 10$), we can recover the outer spiral driven by this $0.3 M_{\text{th}}$ planet in both the $\tau_0 = 1.0$ and 3.0 disks after 3.6 hr of on-source time with the C43-4 + C43-7 configuration pair, and after 8.0 hr of on-source time with the C43-5 + C43-8 pair. Figure 9 shows the former case with $\tau_0 = 1.0$. The contrast (as we have defined contrast, Equation (16)) of the outer spiral driven by the $0.3 M_{\text{th}}$ planet in the adiabatic, $\tau_0 = 1.0$ disk ranges from 0.15–0.3 (see left panel of Figure 4).

The spiral is not clearly visible directly in the synthetic ALMA continuum image, but is recovered in the residuals at $S/N \geq 5$ over $\sim 160^\circ$ of the disk, underscoring the utility of residual maps. We caveat this successful recovery by noting that, although this planet had been living in our hydro simulations for 1500 orbits before we took its picture with ALMA, it created no observable gaps and rings, due to the modest viscosity adopted, $\alpha = 10^{-3}$. As we discuss in the following section, the smoothness of the background disk aids the recovery.

4.4. Can Spirals Be Hiding in Gaps and Rings?

In this section, we explore another possible explanation for the dearth of observed planet-driven spirals despite the

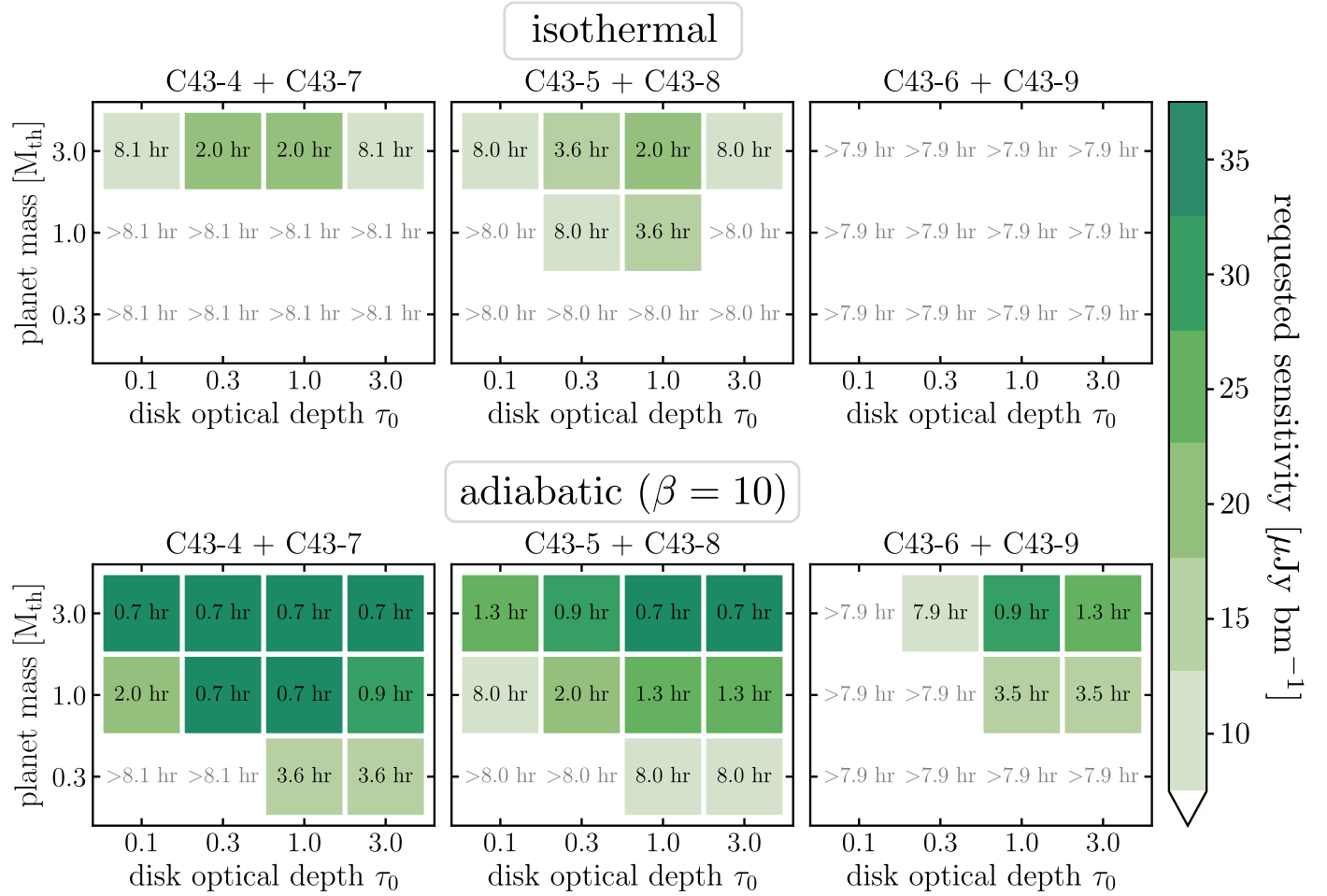


Figure 7. Amount of on-source time required to recover the planet’s outer spiral arm in residuals of our B7 ALMA continuum images under the disk and observing conditions we explore in this work, colored by the corresponding requested sensitivity. White indicates cases where we were not able to recover the spiral.

abundance of observed gaps and rings: Could the presence of the gaps and rings themselves be affecting the observability of the spirals? As discussed in Section 4.1, an observer’s ability to recognize a spiral as a spiral requires seeing it unfurl over a sufficiently large range of azimuth. To span more azimuth $\Delta\phi$, the spiral requires a larger radial breadth Δr of smooth background disk—and this can be affected by gaps and rings.

Figure 10 compares the observability of spirals in a disk with a wide planet-induced gap and narrow outer ring (left panel), to that of a spiral in a disk with a narrower gap and wider outer ring (right panel). To compare the effect of the dust distribution alone, we have re-scaled the underlying intensity maps such that the outer ring in the two disks are equally bright. The left is our optically thinnest ($\tau_0 = 0.1$) disk model and the right is our marginally optically thick ($\tau_0 = 1.0$) disk model, meaning their gas surface densities are different by a factor of 10; as a result, the Stokes number of the $a_{\text{grain}} = 0.14$ mm dust within them is also different by a factor of 10, giving the two disks their different dust distributions. Both disks have an adiabatic equation of state ($\beta = 10$) and embedded planet with mass $M_p = 3.0 M_{\text{th}}$. We show observations made with the C43-6 + C43-9 configuration pair and a combined on-source time of 8.0 hr (achieving measured rms noise $\sim 9.5 \mu\text{Jy beam}^{-1}$) in order to investigate what might be considered a highly desirable observing scenario: high angular resolution and high sensitivity. Atop the observations we overlay $S/N = \pm 5$ contours from the residual maps.

Comparing the two panels in Figure 10, we see that the presence of the wide gap and narrow ring renders a smaller fraction of the spiral visible in the contours. In the left panel, the outer spiral starts farther away from the planet and extends only $\sim 150^\circ$ in azimuth due to the small available radial area. In the right panel, the spiral contour starts closer to the planet and extends a full 270° out to $\sim 2.2 r_p$. Similarly, in the inner disk, there is very little recognizable evidence of a spiral in the left panel, whereas in the right panel we can trace the inner primary arm, the inner secondary arm, and the trough between them.

Like Miranda & Rafikov (2019b), we find that a given planet mass carves shallower gaps in disks with an adiabatic equation of state than in a locally isothermal disk (and this translates to the well-coupled dust distribution, e.g., compare panels (a) versus (e), (b) versus (f), and (d) versus (h) in Figure 5). This is another way that the disk equation of state can affect the observability of spiral arms, in addition to regulating their contrast.

5. Discussion

Inclined disks. While most of our efforts were focused on face-on disks, we briefly experimented with inclined disks as well. Figure 14 in Appendix D shows continuum images and deprojected residual maps for a demonstrative disk, inclined by 30° , 50° , and 70° , along with its original face-on model for comparison. We find that the spiral visibility in the deprojected residual maps is not significantly affected if the disk inclination

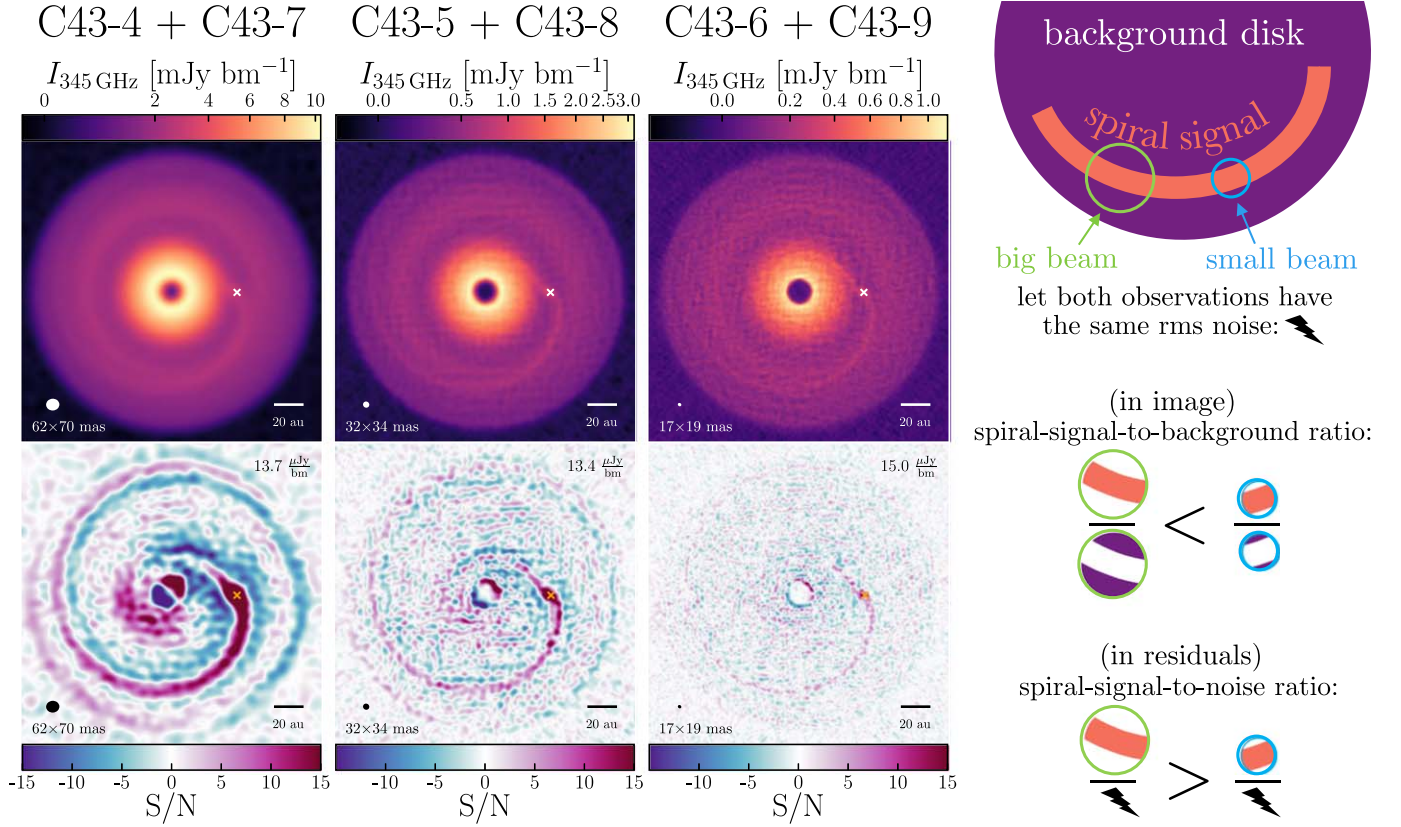


Figure 8. Synthetic ALMA B7 continuum images (top) and residuals (bottom) observed with different configuration pairs, shown from left to right in order of low to high angular resolution, for a $1 M_{\text{th}}$ planet embedded in an adiabatic ($\beta = 10$), marginally optically thick disk ($\tau_0 = 1.0$). In all observations, the measured rms noise (top right corner of residual panels) is very similar. The requested sensitivity is $15 \mu\text{Jy bm}^{-1}$, corresponding to a combined on-source time of 3.5 hr. The schematic (right) shows that a lower angular resolution observation has a lower spiral-signal-to-background ratio (the spiral is *washed out*) but actually has higher spiral S/N (detects the spiral with the highest S/N).

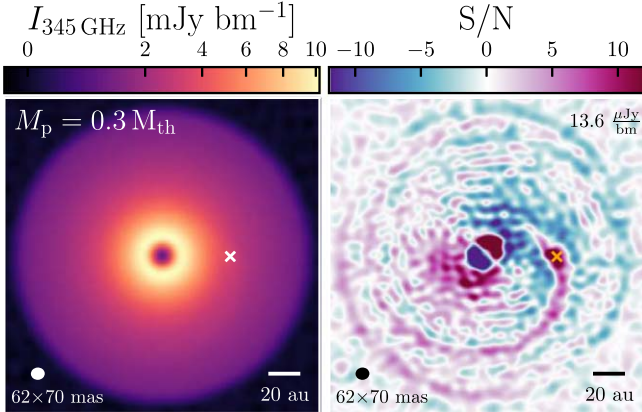


Figure 9. Spiral arm recovery for a low mass planet ($M_p = 0.3 M_{\text{th}} = 1.6 M_{\text{Nep}}$) in a marginally optically thick disk ($\tau_0 = 1.0$) with an adiabatic equation of state ($\beta = 10$), obtained with the combined C43-4 + C43-7 antenna configuration and a combined on-source time of 3.6 hr. The measured rms noise is $13.6 \mu\text{Jy bm}^{-1}$.

is low ($\leq 50^\circ$), but becomes very unclear when the inclination is high ($\geq 70^\circ$). For a given target disk on the sky, the threshold inclination at which a spiral could no longer be as easily recovered in a deprojected residual map would depend on whether the beam resolves the structure along the disk’s minor axis.

Multiwavelength observations. Long-wavelength observations of dust spirals, for example with the ngVLA, may allow

us to probe larger, poorly coupled ($St > St_{\text{crit}}$) dust grains. In Figure 11, we calculate the dust Stokes number of grain sizes relevant to the ngVLA ($a_{\text{grain}} \sim 1\text{--}20\text{ mm}$) and overlay our estimate of the critical Stokes number, St_{crit} (Equation (18)), for a $1.0 M_{\text{th}}$ planet at a disk radius $r = 1.7 r_p$, as found in Section 3.1. The ALMA equivalent of this figure is Figure 2(c). Comparing the spiral morphology in continuum observations of well-coupled versus poorly coupled dust opens new possibilities for future science.

Consider, for example, two observations of the same planet-driven dust spiral—one obtained with ALMA Band 7 ($a_{\text{grain}} \approx 0.14\text{ mm}$) and the second with ngVLA Band 5 ($a_{\text{grain}} \approx 7.0\text{ mm}$). Assuming a local gas surface density of $\sim 3.0\text{ g cm}^{-2}$, these two observations would probe $St = 10^{-2}$ (well-coupled) and $St = 0.4$ (poorly coupled) dust, respectively. These two species are shown in Figure 2(a). At a distance of $0.7 r_p$ outside the planet, our hydrodynamic simulations predict an azimuthal offset between their spiral peaks in surface density of 20° . This is a significant offset that could feasibly be measured in observations.

With a measurement of the azimuthal offset at a given disk radius, and with knowledge of its dependence on the Stokes number from fits to hydro simulations, one could estimate the underlying disk gas surface density, and subsequently measure the disk mass by repeating the exercise at different radii. This would be a direct evaluation of Σ_{gas} and M_{disk} , independent from other methods, and free from the usual uncertainties that stem from making assumptions about the dust-to-gas ratio or

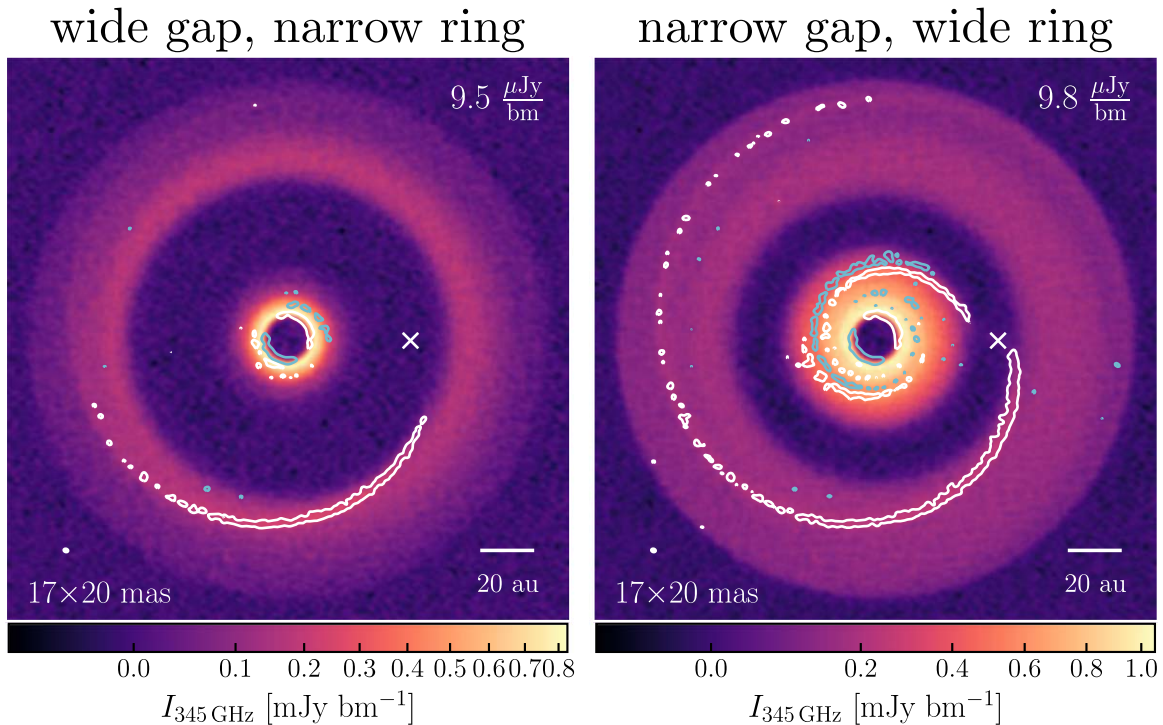


Figure 10. Synthetic ALMA B7 continuum observations exploring the effect of dust gaps and rings on the spiral observability. Both disks are adiabatic ($\beta = 10$) and contain a $3.0 M_{\text{th}} \approx 1.0 M_{\text{Jup}}$ planet; both observations were obtained with the C43-6 + C43-9 configuration pair and 8.0 hr of on-source time. The overlaid white and blue contours are $S/N = +5$ and $S/N = -5$ contours from the residual maps, respectively. The rms noise in each observation is written in the top right corner of the images and the beam size is marked at the lower left corner. Wide gaps and narrow outer rings reduce the amount of disk area over which the spiral can be traced.

dust opacity. We note however that to do this in practice requires taking into account temperature effects, which we discuss in more detail in Appendix B.

Equation of state. One of our main findings is that the observability of dust spirals depends heavily on how much the temperature spiral contributes to the overall spiral intensity, which in turn depends on the cooling timescale. It would therefore be helpful if we had an idea of how quickly we expect disks to cool. As discussed in Section 2.1, typical values of $t_{\text{cool}} = \beta \Omega^{-1}(r)$ span a couple of orders of magnitude above and below unity at different radii within a single disk, and it is also likely that β varies between disks (due to different dust properties, for example). More work is needed to constrain the cooling rate of individual target objects.

In addition to affecting the spiral detectability, the cooling timescale also muddles our ability to deduce the mass of the driving object in an observation because the spiral intensity contrast is degenerate in M_p and β (e.g., Figures 3, 4, and 13). A good understanding of the cooling timescale in specific disks may also help distinguish the two spiral arm excitation mechanisms—we find planet-driven spirals to be more prominent in continuum observations at *longer* cooling timescales ($\beta \geq 10$), whereas spirals driven by gravitational instability have been found to express stronger velocity channel kinks at *shorter* cooling timescales ($\beta \leq 10$; Longarini et al. 2021).

The planet-driven temperature spiral could also have consequences on the radial locations of icelines—again, depending on β . The icelines of common molecules have been found not to correlate with observed locations of gaps (van der Marel et al. 2019). Using radiative cooling, Ziampras et al. (2020) found that shock heating by the planet can raise the disk temperature high enough to displace the water iceline to larger radii. We find that a cooling rate of $\beta = 10^{-1}$ or more

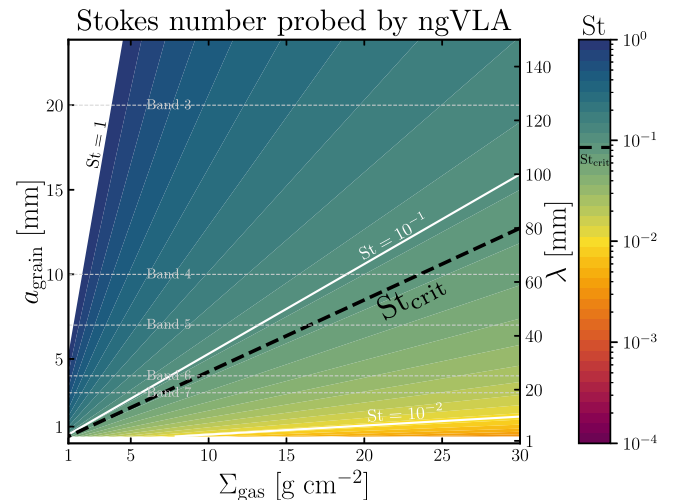


Figure 11. Dust Stokes number calculated for a range of gas surface densities and ngVLA dust grain sizes. For typical observing wavelengths of each ngVLA band, we mark the grain size probed assuming (LH y-axis) $a_{\text{grain}} = \lambda_{\text{obs}}/2\pi$ (RH y-axis). Long-wavelength observations with the ngVLA provide access to the $St > St_{\text{crit}}$ regime.

is required for a $1.0 M_{\text{th}}$ planet to drive a *spiral* whose peak temperature is transiently $>10\%$ of the background (Figure 13 in Appendix C), but that to get an azimuthally averaged *ring* of 5% temperature enhancement over the background outside the planet, a $\beta = 10^2$ and a $3.0 M_{\text{th}}$ planet on a fixed orbit are needed (not shown).

Comparison to other published synthetic continuum images. To our knowledge no previous theoretical works have specifically targeted the observability of planet-driven dust spirals in the ALMA continuum, but a few have provided synthetic ALMA

continuum images of planet-hosting disks for alternative purposes—and in some cases planet-driven dust spirals are visible in their results.

The image in Table 5 of Szulágyi et al. (2018) shows a model almost identical to one of our runs: a Band 7 continuum observation with a $1.0 M_{\text{Jup}}$ planet at 52 au and measured rms noise of $15 \mu\text{Jy bm}^{-1}$, though with the C50-28 configuration (i.e., assuming future antennas). As in our case (e.g., Figure 7), the outer primary spiral arm is directly visible in their image. They used the radiative 3D hydrodynamics code JUPITER (which includes heating by viscosity and adiabatic compression, and cooling by radiation and adiabatic expansion), and also emphasized that the temperature of one’s target planet signature (in their case the circumplanetary disk) influences its observability. They assumed, like us, $T_{\text{dust}} = T_{\text{gas}}$, and unlike us, obtained their dust surface density distribution by scaling the gas (though for ALMA B7 this is a valid assumption; see Figure 2(c)).

Nazari et al. (2019) showed Band 7 observations achieving an rms noise of $18.5 \mu\text{Jy bm}^{-1}$ for our medium angular resolution configuration pair, C43-5 + C43-8, of a disk with a low mass embedded planet ($30 M_{\oplus}$, equivalent to 90% our $0.3 M_{\text{th}}$ planet). They reported that no spirals were visible in their images. This agrees with our result in Figure 9 (with a slightly better rms noise of $13.6 \mu\text{Jy bm}^{-1}$), where we showed that a residual map is needed to detect the spiral.

In residual maps of Band 6 observations of disks with a locally isothermal equation of state, spatially and temporally constant Stokes number, and two embedded $\geq 2.5 M_{\text{th}}$ planets, Veronesi et al. (2019) were able to detect the outer planet’s inner primary and secondary spiral arm. In contrast to our parameter space, their outer planet was placed at 145 au.

Rowther et al. (2020) investigated the influence of a migrating planet embedded in a gravitationally unstable disk in which β varies radially with PHANTOM SPH simulations. They calculated their Band 6 ALMA continuum residuals using the same method as us, and found that spiral arms driven by an inwardly migrating $3.0 M_{\text{Jup}}$ planet initially at 160 au were visible in both face-on and 40° inclined disks after >1 hr of integration time. They too found that a lower angular resolution observation, with its higher S/N, allowed the planet-driven spirals to be seen more easily (see our Figure 8), though there they were comparing the C43-6 and C43-7 configurations unpaired. We provide B7 images obtained with individual configurations in Figure 16 in Appendix E.

Caveats. Our work could benefit from a few improvements to incorporate more realistic physics. We have restricted the planet to be on the simplest orbit, i.e., circular, coplanar, and non-migrating. Relaxing these assumptions may affect the morphology of the gap(s) (Meru et al. 2019; Nazari et al. 2019; Pérez et al. 2019; Weber et al. 2019) and the spirals (Quillen et al. 2003; Duffell & Chiang 2015), and impact the observability of spirals at a quantitative level. For example, Kanagawa et al. (2021) showed that the relative positions between the planet and the dust rings at gap edges depend on the migration rate of the planet. Meanwhile, the dust may be puffed up vertically in spirals (Krapp et al. 2022), which may result in detectable signatures in continuum observations (Doi & Kataoka 2021). It is impossible to capture such effects in our 2D simulations. In addition, the presence of multiple planets, as in the case of PDS 70 (Haffert et al. 2019), may also complicate the recognition of individual spirals.

We have ignored the effect of dust scattering, which can be important in optically thick disks (Kataoka et al. 2015; Zhu et al. 2019; Liu 2019). While we mainly focus on optically thin to marginally optically thick cases, scattering may cause an order unity correction to the overall disk brightness when $\tau \sim 1$ if the dust albedo is close to 1 (Figure 1 in Sierra & Lizano 2020), thus affecting the expected integration time to reach a desired S/N. As a detailed sidenote, the increased dust surface density (thus τ) locally at the spirals would introduce another correction factor, but we expect its impact on the spiral contrast to also be minimal as the spiral Σ_{dust} enhancements are only on the order of 10%.

Finally, we adopt a single dust size most sensitively probed in observations with a fixed initial dust-to-gas mass ratio. In real systems, some dust mass is expected to be in grains of other sizes and thus does not contribute significantly to observations at a particular wavelength (Birnstiel et al. 2018). As such, the disk brightness in our models might be taken as upper (more optimistic) limits for our assumed initial dust-to-gas mass ratio (0.01).

6. Summary and Conclusions

Detecting a planet’s spiral wake would constitute compelling evidence for its presence in the disk—particularly if the inferred planet-spiral configuration is consistent with other signposts of the planet such as gaps/rings or local velocity kinks. In this work, we carry out 2D gas + dust hydrodynamic simulations and radiative transfer calculations. We produce synthetic Band 7 ALMA continuum observations of planet-driven dust spirals under a wide variety of disk and observing conditions. Our goal is to advise the search for planet-driven spirals in existing and future ALMA observations by identifying the most promising disk environments and observing specifications. We discuss the important physics underlying the observability of dust spirals in Section 3 before presenting our simulated observations in Section 4. Our conclusions are as follows:

1. The critical Stokes number St_{crit} dividing the well-coupled and poorly coupled dust regimes can be estimated by equating the dust’s intrinsic stopping time t_{stop} with the gas spiral wake crossing time t_{cross} (Equation (17)). We find $St_{\text{crit}} \sim 0.05 - 0.1$ (Equation (18)). Dust particles with $St < St_{\text{crit}}$ form spirals identical to the driving gas spiral in morphology, while bigger particles azimuthally lag behind the gas peaks (Figures 2(a), (b)), echoing Sturm et al. (2020). At almost all gas surface densities and observing wavelengths, ALMA probes well-coupled ($St < St_{\text{crit}}$) dust. Therefore, barring inclination or geometrical offsets, we expect dust spirals observed with ALMA to be excellent tracers of gas spirals at the midplane (Figure 2(c)).
2. While the surface density contrast of well-coupled dust spirals depends non-monotonically on the cooling time-scale β and is the largest in locally isothermal disks, the strength of the temperature spiral formed in adiabatic disks increases monotonically with β . Adiabatic disks that cool slowly ($\beta \geq 10$) produce the hottest spirals with the largest contrast in surface brightness (Figures 3 and 13).
3. The difference in brightness between dust spirals in slowly cooling versus locally isothermal disks is most pronounced when the disk is optically thick (Figure 4).

4. The signal of a spiral in a continuum image can be effectively highlighted in the residual map, enabling detections that otherwise may go unnoticed (Figures 5 and 6).
5. Planet-driven dust spirals are easiest to detect in adiabatic disks that cool slowly ($\beta \gtrsim 10$), that are marginally but not too optically thick ($\tau_0 \gtrsim 1.0$), and that host massive planets ($M_p \gtrsim 1.0 M_{\text{th}}$). In such disks, spirals can be detected with integration times on the order of hours (Figure 7).
6. Detecting a spiral is not contingent on resolving it. Higher angular resolution observations (beam size $\approx 0.5 \times$ the spiral width) have a higher spiral-signal-to-background ratio (they contain a greater proportion of spiral signal within each beam), but have a lower spiral S/N. Lower angular resolution observations (beam size $\approx 2 \times$ the spiral width) wash out the spiral signal in the continuum image itself, but reveal the spiral with higher S/N in a residual map (Figure 8).
7. In a face-on, adiabatic ($\beta = 10$) marginally optically thick disk with a smooth dust surface density distribution exterior to the planet, we recover the outer spiral arm driven by a 1.6 Neptune mass planet ($0.3 M_{\text{th}}$) around a solar-type star at 50 au in the residuals of a Band 7 continuum observation obtained with an angular resolution of 62×70 mas and a measured rms noise of $13.6 \mu\text{Jy beam}^{-1}$, achievable with 3.6 hr of on-source time and a full continuum bandwidth of 7.5 GHz (Figure 9).
8. The presence of gaps and rings can impair the observability of colocated spirals, by reducing the amount of disk area over which the spiral can be traced (Figure 10).

Future continuum observations with the ngVLA may provide access to the poorly coupled ($St > St_{\text{crit}}$) dust spiral regime (Figure 11). Comparing the azimuthal location of dust spiral peaks in ALMA versus ngVLA observations and measuring their offsets (Figure 2(a)) may enable direct constraints on the gas surface density and disk mass.

We are grateful to an anonymous referee for constructive suggestions that improved our paper. J.S. thanks Pablo Benítez-Llambay and Leonardo Krapp for maintaining and monitoring the public FARGO3D Bitbucket, and Shangjia Zhang and Dhruv Muley for providing simulations—all of which aided in code comparisons; Ardjan Sturm for consultation where our works overlap; Sarah Wood at the ALMA Help Desk and Nienke van der Marel for technical advice with the ALMA OT; Jeff Jennings and Brodie Norfolk for technical help on uv tables; and the Planet Formation Group at the University of Victoria for helpful discussions. Hydrodynamic simulations were performed on GPU computing nodes of Graham, Béluga and Cedar hosted by Compute Canada (www.computeCanada.ca), as well as GASTRO hosted at McMaster University. R.D. and J.S. are supported by the Natural Sciences and Engineering Research Council of Canada (NSERC) and the Alfred P. Sloan Foundation. R.A.B. was supported by a Royal Society University Research Fellowship, the STFC consolidated grant ST/S000623/1 and funding from the European Research Council (ERC) under the European Union’s Horizon 2020 research and innovation programmes PEVAP (grant agreement No. 853022) and DUSTBUSTERS (grant agreement No. 823823).

Software: astropy (Astropy Collaboration et al. 2013, 2018), CASA (McMullin et al. 2007), CMasher (van der Velden 2020), matplotlib (Hunter 2007), NumPy (Harris et al. 2020), pandas (McKinney 2011), SciPy (Virtanen et al. 2020).

Data availability: full set of synthetic ALMA observations and an image gallery are available at FigShare: [10.6084/m9.figshare.19148912](https://figshare.com/19148912).

Appendix A Representative Disk Radial Profiles

Figure 12 illustrates the differences between our $\tau_0 = 0.1, 0.3, 1.0,$ and 3.0 models by showing azimuthally averaged radial profiles of the relevant disk quantities (for one

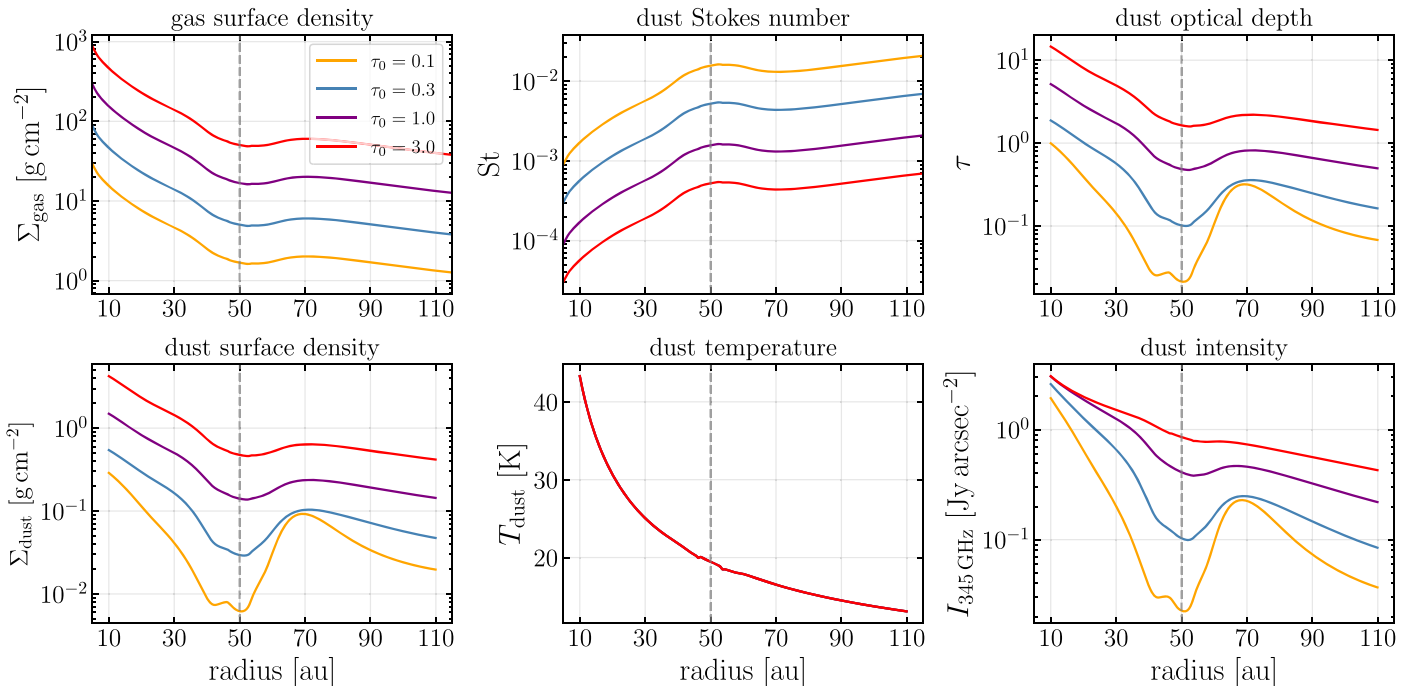


Figure 12. Azimuthally averaged radial profiles of important disk quantities for four of our models, demonstrating the construction of the optical depth parameter, τ_0 . Shown is the adiabatic ($\beta = 10$) disk with a $1.0 M_{\text{th}}$ embedded planet.

demonstrative permutation of equation of state and M_p). As described in Section 2.2, four hydrodynamic simulations are run and normalized individually such that the dust surface density (with an initial profile determined by a fixed dust-to-gas ratio of 0.01) gives an initial optical depth at r_p of 0.1, 0.3, 1.0, and 3.0. By fixing the grain size to $a_{\text{grain}} = 0.14 \mu\text{m}$, the Stokes number is different in each disk by the same factor as the gas surface density (Section 4.4).

Appendix B

On Assuming Dust and Gas Thermal Equilibrium At the Midplane

As described in Section 2.2, we use the gas temperature output of our adiabatic FARGO3D hydrodynamic simulations as the dust temperature input for our radiative transfer calculations and subsequent ALMA observations of planet-driven dust spirals in adiabatic disks. Below, we justify this assumption and describe considerations for observers interested in longer wavelength observations (see discussion around Figure 11 in Section 5).

Under what conditions should the dust temperature T_{dust} be equal to the gas temperature T_{gas} ? The argument is simple: the temperature of a dust particle will be equal to that of its surroundings if it spends enough time in those surroundings to equilibrate. We will show that the time it takes a dust particle to respond thermally happens to be very similar to the time it takes to respond aerodynamically, $t_{\text{therm}} \approx t_{\text{stop}}$. Dust that is well coupled to the gas, as in our simulations, is therefore also well thermally coupled.

Consider a dust particle, with stopping time t_{stop} and thermal coupling time t_{therm} , flowing through a gas spiral wake with crossing time t_{cross} (Equation (17)). First, we express the particle's stopping time as

$$t_{\text{stop}} = \frac{\rho_{\text{dust}} a_{\text{grain}}}{\rho_{\text{gas}} v_{\text{th}}}, \quad (\text{B1})$$

where ρ_{dust} and ρ_{gas} are the dust and gas volume densities, a_{grain} is the dust grain size and $v_{\text{th}} = \sqrt{8k_B T_{\text{gas}} / \pi \mu m_H}$ is the mean thermal speed of the gas molecules. As the particle enters the spiral wake, the temperature of its surroundings changes (e.g., Figure 3). The heating rate of a dust grain is given by (e.g., Burke & Hollenbach 1983)

$$m_{\text{dust}} C_{\text{dust}} \frac{\partial T_{\text{dust}}}{\partial t} = \pi a_{\text{grain}}^2 n_{\text{gas}} v_{\text{th}} \alpha (2k_B T_{\text{gas}} - 2k_B T_{\text{dust}}), \quad (\text{B2})$$

where α is the accommodation coefficient, m_{dust} and C_{dust} are the mass and specific heat capacity of the particle, n_{gas} is the gas number density, and k_B is Boltzmann's constant. This may be written as

$$\frac{\partial T_{\text{dust}}}{\partial t} = \left[\frac{4\pi a_{\text{grain}}^2 \rho_{\text{gas}} v_{\text{th}}}{3m_{\text{dust}}} \right] \frac{3k_B}{2C_{\text{dust}}} \alpha (T_{\text{gas}} - T_{\text{dust}}). \quad (\text{B3})$$

Identifying the terms in square parentheses with $1/t_{\text{stop}}$, we arrive at

$$\frac{\partial T_{\text{dust}}}{\partial t} = \frac{1}{t_{\text{stop}}} \frac{3k_B}{2C_{\text{dust}}} \alpha (T_{\text{gas}} - T_{\text{dust}}). \quad (\text{B4})$$

We may thus define the thermal coupling time as

$$t_{\text{therm}} = t_{\text{stop}} \times \frac{2C_{\text{dust}}}{3k_B} \alpha^{-1}. \quad (\text{B5})$$

Since $\alpha \approx 1$ (Burke & Hollenbach 1983), the particle's thermal coupling time will be similar to its stopping time $t_{\text{stop}} \approx t_{\text{therm}}$ if the specific heat capacity of the dust and gas are similar. Requiring enough time for a particle to come into thermal equilibrium with the gas inside the spiral wake, i.e., requiring $t_{\text{therm}} < t_{\text{cross}}$, is therefore equivalent to requiring $t_{\text{stop}} < t_{\text{cross}}$, which is our definition of being well coupled, $\text{St} < \text{St}_{\text{crit}}$ (Section 3.1). In other words, small dust grains probed by ALMA will have the same temperature as the gas. Their temperature spirals, and their intensity spirals, will be collocated.

The temperature spiral peaks of gas and poorly coupled ($\text{St} > \text{St}_{\text{crit}}$, and therefore $t_{\text{therm}} > t_{\text{cross}}$) dust will *not* be collocated. For observers interested in measuring the azimuthal offset between dust spirals in ALMA versus ngVLA observations, this is a good thing; if the dust temperature peaks were aligned with that of the gas, the azimuthal offset between gas and large dust in the observed surface brightness would be reduced from that in surface density. Whether the poorly coupled dust temperature spiral peaks align with *their own* surface density peaks requires future investigation, but it is promising that they are at least governed by similar timescales, $t_{\text{therm}} \approx t_{\text{stop}}$.

Appendix C

An Alternative Visualization of Figure 3

Figure 13 is an alternative visualization of Figure 3, in which we trace the perturbation peaks in dust surface density, temperature, and intensity (in the optically thin limit) along

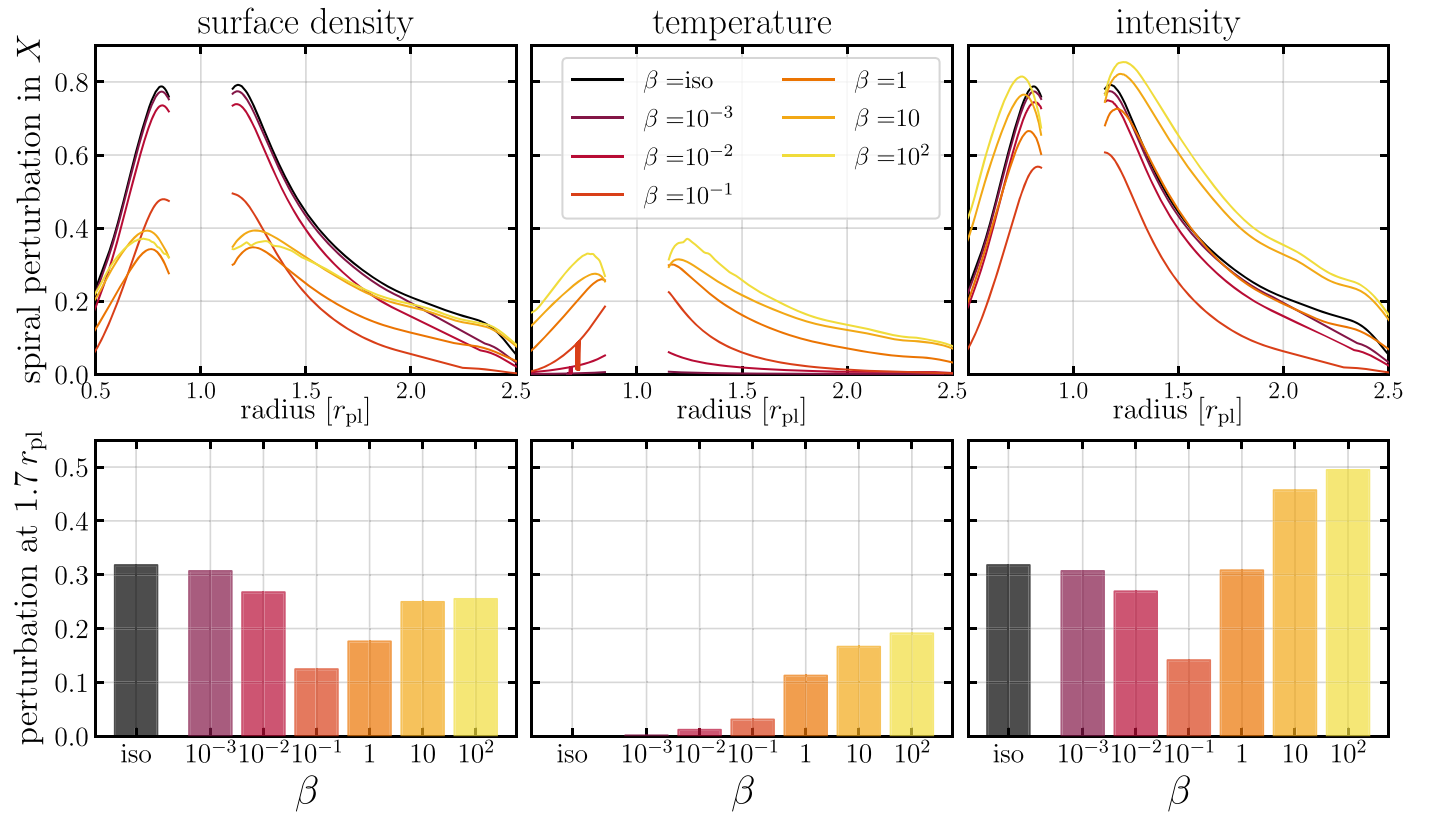


Figure 13. Like Figure 3, but with the perturbations in each disk quantity traced along the inner and outer primary arms (top panels), and showing additional cooling timescales β . To highlight the non-monotonic dependence of the dust surface density and intensity perturbations on β , as well as to emphasize the spread in the amplitude generated by a given planet mass under different β , we show the values at $1.7 r_{\text{p}}$ as a bar chart (bottom panels). In this case the planet mass is $1.0 M_{\text{th}}$.

the inner and outer primary arms. We resolve the dependence of these quantities on the cooling timescale β with additional values not shown in Figure 3. The amplitude of the perturbations varies substantially for the same $1.0 M_{\text{th}}$ embedded planet.

Appendix D Synthetic Observations of Inclined Disks

As a first start in informing observations of inclined disk systems, we generate an additional set of continuum images of tilted disks. The underlying dust surface density and temperature maps have been *squished* along the north–south axis by a factor of $\cos(i)$, and the dust surface density scaled by a factor of $1/\cos(i)$, before the emergent dust intensity was calculated.

The optical depths of the inclined disks are thus different to their face-on counterparts, but we still use the τ_0 parameter to refer to them.

We also experimented with changing the position angle of the planet by 90° (such that it was located on the north–south axis) and found that the spiral visibility in the deprojected residual maps was not greatly affected.

The images in Figure 14 depict a $M_{\text{p}} = 1.0 M_{\text{th}}$ planet embedded in an optically thin ($\tau_0 = 0.1$) disk with an adiabatic equation of state ($\beta = 10$), observed with the C43-5 + C43-8 configuration pair for a combined on-source time of 8.02 hr. The synthesized beam is shown in the bottom left corner of each image, and the measured rms noise is shown in the top left corner of the deprojected residual panels. View all our model permutations at FigShare: [10.6084/m9.figshare.19148912](https://figshare.com/figures-and-data/10.6084/m9.figshare.19148912).

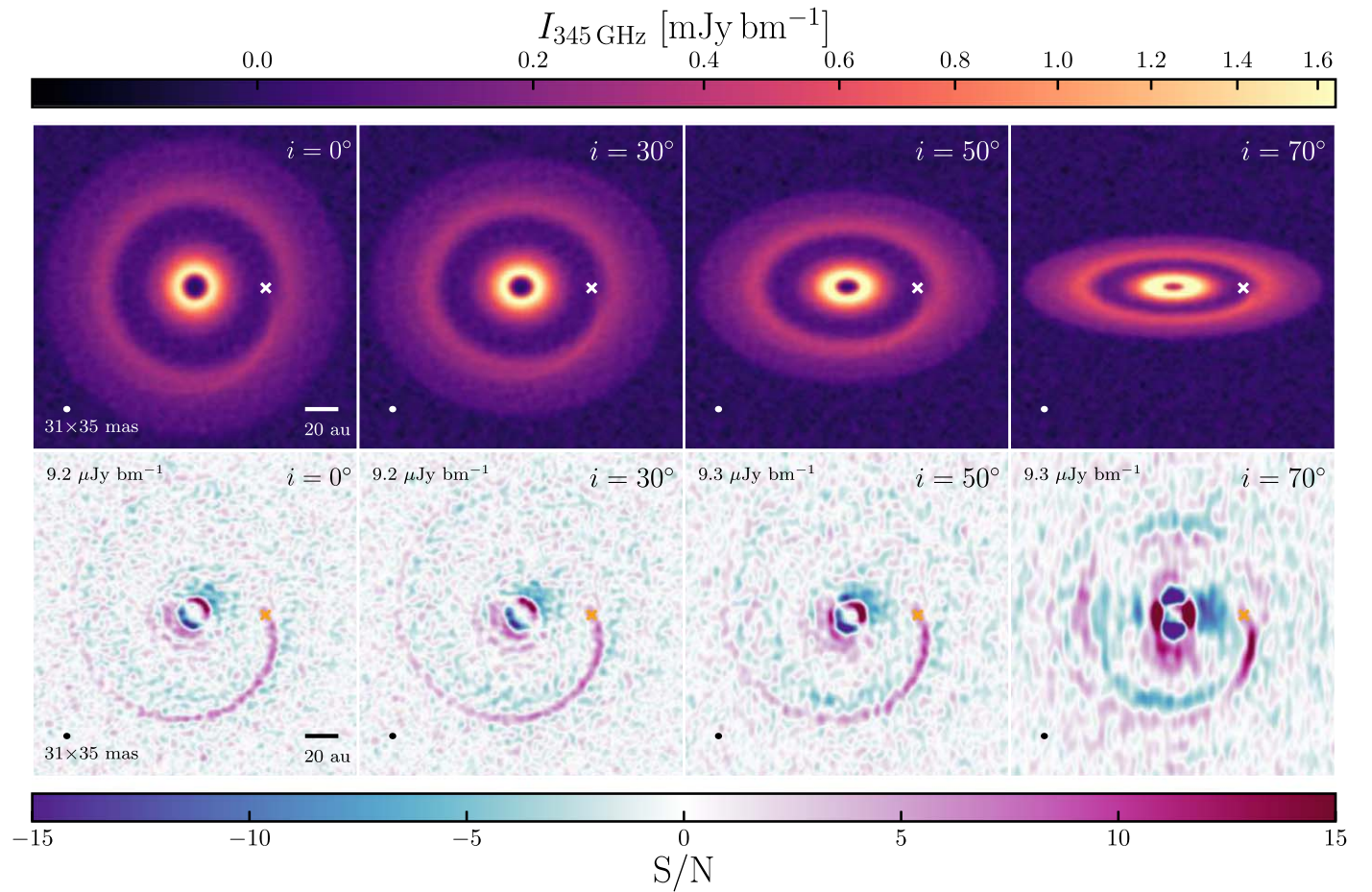


Figure 14. Synthetic ALMA B7 continuum images (top) and deprojected residuals (bottom) of a demonstrative model disk, inclined by 30° , 50° , and 70° to compare spiral visibility under varying disk inclination. The effect of inclination is not significant unless the disk is very inclined (i.e., 70° , rightmost column).

Appendix E Considerations Behind Synthetic Observations

In Table 1 we provide the individual and combined on-source (OS) times used in this work, which were specified by the ALMA Cycle 8 OT as what is needed to achieve each selected requested continuum sensitivity with each configuration pair at 345 GHz for a bandwidth of 7.5 GHz. For context, we also show the total observing time including overheads (OT), which does not scale linearly with the estimated time on source. Our highest sensitivity observation requires eight scheduling block executions.

As described in Section 4, we experimented with using `frank` (Jennings et al. 2020) to create residual maps and highlight the planet-driven spiral signal in our synthetic continuum observations. We fitted the observed visibilities with `frank` (exploring 16 permutations of the hyperparameters w_{smooth} and α and using the corrected weights), converted the residual uv table into a measurement set, and imaged that measurement set with `tclean` in a way identical to as was done for the synthetic continuum observations, with the exception of setting the number of iterations to zero. Figure 15 provides a comparison between `frank` and our method of calculating residuals directly in the image plane (e.g., Figure 6). We found that with the corrected weights, the visibility residuals were most similar to our image plane residuals, and were very insensitive to w_{smooth} and α . Figure 15

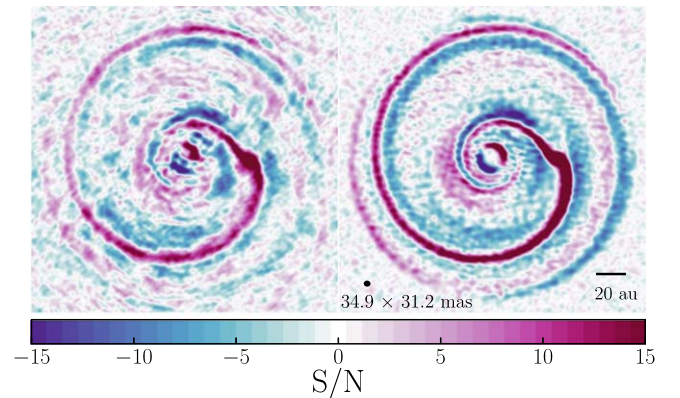


Figure 15. Left: imaged `frank` visibility residuals generated with parameters that best revealed the planet-driven spiral of the parameters that we explored. Right: residuals generated with the method used in this work. The measurement set shared between these two images corresponds to the model that was presented in panel (h) of Figures 5 and 6 and represents one of the strongest spiral recoveries out of our full set of 432 face-on model images.

shows the results with parameters $w_{\text{smooth}} = 1.01$, $\alpha = 1.05$, and $R_{\text{max}} = 1''2$.

In Figure 16 we show continuum observations made from the compact and extended configuration measurement sets that were concatenated to create the continuum images presented in the middle column of Figure 8. The individual measurement sets were imaged by the same procedure as was their

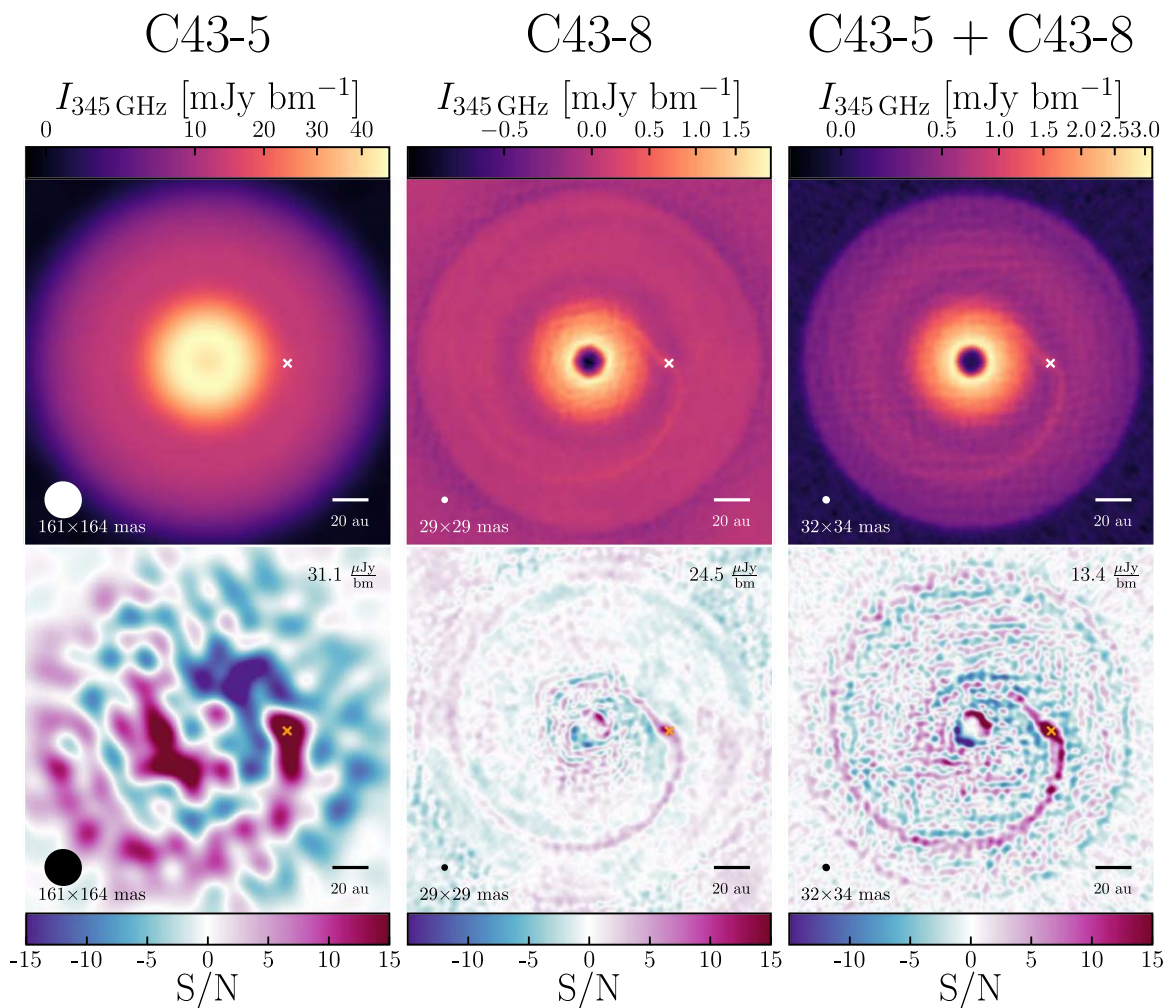


Figure 16. Synthetic ALMA B7 continuum observations with the compact and extended configurations that correspond to the pair shown in the middle column of Figure 8. Following the Sensitivity Calculator in the ALMA OT, the combined on-source time of 3.56 hr for this requested sensitivity of $15 \mu\text{Jy bm}^{-1}$ was distributed as 0.64 hr with C43-5 and 2.92 hr with C43-8 (see also Table 1). The measured rms noise in each observation is written in the top right corner of the residual maps.

combination. The residual maps of the extended configuration observation demonstrate the long baseline artifacts mentioned in Section 2.3. These artifacts can be generally characterized as

repeating patterns of large regions on the sky with over- or under-intensity, in the rough shape of stripes, slices of pie, or wide spokes, depending on the configuration.

Table 1
ALMA Observing Time for Requested Sensitivities

Requested Sensitivity ($\mu\text{Jy bm}^{-1}$)	Compact On source (hr)	Extended On source (hr)	Combined	
			OS (hr)	OS+OH (hr)
	C43-4	C43-7		
10	1.51	6.57	8.08	18.51
15	0.67	2.92	3.59	8.35
20	0.38	1.64	2.02	4.63
25	0.24	1.05	1.29	3.15
30	0.17	0.73	0.90	2.09
35	0.12	0.53	0.66	1.62
	C43-5	C43-8		
10	1.45	6.57	8.02	21.94
15	0.64	2.92	3.56	10.08
20	0.36	1.64	2.00	5.49
25	0.23	1.05	1.28	4.03
30	0.16	0.73	0.89	2.52
35	0.12	0.53	0.65	2.08
	C43-6	C43-9		
10	1.38	6.57	7.95	18.21
15	0.61	2.92	3.53	8.22
20	0.34	1.64	1.98	4.55
25	0.22	1.05	1.27	3.10
30	0.15	0.73	0.88	2.06
35	0.11	0.53	0.65	1.60

Note. Since the C43-6 + C43-9 configuration pair was not available in Cycle 8, the Cycle 7 ALMA OT was used to determine the observing times for that pair.

ORCID iDs

Jessica Speedie  <https://orcid.org/0000-0003-3430-3889>
 Richard A. Booth  <https://orcid.org/0000-0002-0364-937X>
 Ruobing Dong (董若冰)  <https://orcid.org/0000-0001-9290-7846>

References

- Andrews, S. M., Huang, J., Pérez, L. M., et al. 2018, *ApJL*, 869, L41
 Arzamasskiy, L., & Rafikov, R. R. 2018, *ApJ*, 854, 84
 Astropy Collaboration, Price-Whelan, A. M., Sipőcz, B. M., et al. 2018, *AJ*, 156, 123
 Astropy Collaboration, Robitaille, T. P., Tollerud, E. J., et al. 2013, *A&A*, 558, A33
 Bae, J., & Zhu, Z. 2018a, *ApJ*, 859, 118
 Bae, J., & Zhu, Z. 2018b, *ApJ*, 859, 119
 Bae, J., Zhu, Z., & Hartmann, L. 2017, *ApJ*, 850, 201
 Beckwith, S. V. W., Sargent, A. I., Chini, R. S., & Guesten, R. 1990, *AJ*, 99, 924
 Benítez-Llambay, P., & Masset, F. S. 2016, *ApJS*, 223, 11
 Birmstiel, T., Dullemond, C. P., Zhu, Z., et al. 2018, *ApJL*, 869, L45
 Boccaletti, A., Pantin, E., Ménard, F., et al. 2021, *A&A*, 652, L8
 Booth, R. A., Sijacki, D., & Clarke, C. J. 2015, *MNRAS*, 452, 3932
 Brown-Sevilla, S. B., Keppler, M., Barraza-Alfaro, M., et al. 2021, *A&A*, 654, A35
 Casassus, S., Christiaens, V., Cárcamo, M., et al. 2021, *MNRAS*, 507, 3789
 Burke, J. R., & Hollenbach, D. J. 1983, *ApJ*, 265, 223
 de Val-Borro, M., Edgar, R. G., Artymowicz, P., et al. 2006, *MNRAS*, 370, 529
 Doi, K., & Kataoka, A. 2021, *ApJ*, 912, 164
 Dong, R., & Fung, J. 2017, *ApJ*, 835, 146
 Dong, R., Li, S., Chiang, E., & Li, H. 2017, *ApJ*, 843, 127
 Dong, R., Li, S., Chiang, E., & Li, H. 2018a, *ApJ*, 866, 110
 Dong, R., Liu, S.-y., Eisner, J., et al. 2018c, *ApJ*, 860, 124
 Dong, R., Najita, J. R., & Brittain, S. 2018b, *ApJ*, 862, 103
 Dong, R., Rafikov, R. R., & Stone, J. M. 2011a, *ApJ*, 741, 57
 Dong, R., Rafikov, R. R., Stone, J. M., & Petrovich, C. 2011b, *ApJ*, 741, 56
 Duffell, P. C., & Chiang, E. 2015, *ApJ*, 812, 94
 Fung, J., & Chiang, E. 2016, *ApJ*, 832, 105
 Fung, J., Shi, J.-M., & Chiang, E. 2014, *ApJ*, 782, 88
 Garaud, P., Barrière-Fouchet, L., & Lin, D. N. C. 2004, *ApJ*, 603, 292
 Goldreich, P., & Tremaine, S. 1978, *ApJ*, 222, 850
 Goldreich, P., & Tremaine, S. 1979, *ApJ*, 233, 857
 Goldreich, P., & Tremaine, S. 1980, *ApJ*, 241, 425
 Haffert, S. Y., Bohn, A. J., de Boer, J., et al. 2019, *NatAs*, 3, 749
 Harris, C. R., Millman, K. J., van der Walt, S. J., et al. 2020, *Natur*, 585, 357
 Huang, J., Andrews, S. M., Dullemond, C. P., et al. 2018a, *ApJL*, 869, L42
 Huang, J., Andrews, S. M., Pérez, L. M., et al. 2018b, *ApJL*, 869, L43
 Hunter, J. D. 2007, *CSE*, 9, 90
 Jennings, J., Booth, R. A., Tazzari, M., Clarke, C. J., & Rosotti, G. P. 2022, *MNRAS*, 509, 2780
 Jennings, J., Booth, R. A., Tazzari, M., Rosotti, G. P., & Clarke, C. J. 2020, *MNRAS*, 495, 3209
 Kanagawa, K. D., Muto, T., & Tanaka, H. 2021, *ApJ*, 921, 169
 Kataoka, A., Muto, T., Momose, M., et al. 2015, *ApJ*, 809, 78
 Krapp, L., Kratter, K. M., & Youdin, A. N. 2022, *ApJ*, 928, 156
 Kraus, S., Kreplin, A., Fukugawa, M., et al. 2017, *ApJL*, 848, L11
 Kurtovic, N. T., Pérez, L. M., Benisty, M., et al. 2018, *ApJL*, 869, L44
 Liu, H. B. 2019, *ApJL*, 877, L22
 Longarini, C., Lodato, G., Toci, C., et al. 2021, *ApJL*, 920, L41
 Mawet, D., Absil, O., Montagnier, G., et al. 2012, *A&A*, 544, A131
 McKinney, W. 2011, Python for High Performance and Scientific Computing, Vol. 14, 1
 McMullin, J. P., Waters, B., Schiebel, D., Young, W., & Golap, K. 2007, in ASP Conf. Ser., 376, Astronomical Data Analysis Software and Systems XVI, ed. R. A. Shaw, F. Hill, & D. J. Bell (San Francisco, CA: ASP), 127
 McNally, C. P., Nelson, R. P., Paardekooper, S.-J., & Benítez-Llambay, P. 2019, *MNRAS*, 484, 728
 Meru, F., Juhász, A., Ilee, J. D., et al. 2017, *ApJL*, 839, L24
 Meru, F., Rosotti, G. P., Booth, R. A., Nazari, P., & Clarke, C. J. 2019, *MNRAS*, 482, 3678
 Miranda, R., & Rafikov, R. R. 2019a, *ApJ*, 875, 37
 Miranda, R., & Rafikov, R. R. 2019b, *ApJL*, 878, L9
 Miranda, R., & Rafikov, R. R. 2020a, *ApJ*, 904, 121
 Miranda, R., & Rafikov, R. R. 2020b, *ApJ*, 892, 65
 Muley, D., Dong, R., & Fung, J. 2021, *AJ*, 162, 129
 Nazari, P., Booth, R. A., Clarke, C. J., et al. 2019, *MNRAS*, 485, 5914
 Ogilvie, G. I., & Lubow, S. H. 2002, *MNRAS*, 330, 950
 Paneque-Carreño, T., Pérez, L. M., Benisty, M., et al. 2021, *ApJ*, 914, 88
 Pavlyuchenkov, Y., Akimkin, V., Wiebe, D., & Vorobyov, E. 2019, *MNRAS*, 486, 3907
 Pérez, S., Casassus, S., Baruteau, C., et al. 2019, *AJ*, 158, 15
 Quillen, A. C., Varniere, P., Minchev, I., & Frank, A. 2003, arXiv:astro-ph/0312647
 Ren, B., Dong, R., van Holstein, R. G., et al. 2020, *ApJL*, 898, L38
 Rosotti, G. P., Benisty, M., Juhász, A., et al. 2020, *MNRAS*, 491, 1335
 Rosotti, G. P., Juhász, A., Booth, R. A., & Clarke, C. J. 2016, *MNRAS*, 459, 2790
 Rowther, S., Meru, F., Kennedy, G. M., Nealon, R., & Pinte, C. 2020, *ApJL*, 904, L18
 Shakura, N. I., & Sunyaev, R. A. 1973, *A&A*, 500, 33
 Sierra, A., & Lizano, S. 2020, *ApJ*, 892, 136
 Sturm, J. A., Rosotti, G. P., & Dominik, C. 2020, *A&A*, 643, A92
 Szulágyi, J., Plas, G. v. d., Meyer, M. R., et al. 2018, *MNRAS*, 473, 3573
 Takeuchi, T., & Lin, D. N. C. 2002, *ApJ*, 581, 1344
 van der Marel, N., Dong, R., di Francesco, J., Williams, J. P., & Tobin, J. 2019, *ApJ*, 872, 112
 van der Velden, E. 2020, *JOSS*, 5, 2004
 Veronesi, B., Lodato, G., Dipierro, G., et al. 2019, *MNRAS*, 489, 3758
 Virtanen, P., Gommers, R., Oliphant, T. E., et al. 2020, *NatMe*, 17, 261
 Weber, P., Pérez, S., Benítez-Llambay, P., et al. 2019, *ApJ*, 884, 178
 Whipple, F. L. 1972, in From Plasma to Planet, Proc. of the 21st Nobel Symp., ed. A. Elvius (New York: Wiley Interscience Division), 211
 Zhang, S., & Zhu, Z. 2020, *MNRAS*, 493, 2287
 Zhang, S., Zhu, Z., Huang, J., et al. 2018, *ApJL*, 869, L47
 Zhu, Z., Dong, R., Stone, J. M., & Rafikov, R. R. 2015, *ApJ*, 813, 88
 Zhu, Z., Zhang, S., Jiang, Y.-F., et al. 2019, *ApJL*, 877, L18
 Ziampras, A., Ataiee, S., Kley, W., Dullemond, C. P., & Baruteau, C. 2020, *A&A*, 633, A29